University of Nevada, Reno

NEAR-SURFACE AIR TEMPERATURE IN COMPLEX TERRAIN: DAILY PREDICTIONS OF FINE-SCALE (30 M) TEMPERATURE IN THE SNAKE RANGE, NEVADA, USA

A Thesis Submitted in Partial Fulfillment

of the Requirements for the Degree of Master of Science in

Geography

by

Andrew P. Vitale

Dr. Thomas P. Albright / Thesis Advisor

May 2015

**UNIVERSITY
OF NEVADA
RENO**

THE GRADUATE SCHOOL

We recommend that the thesis prepared
under our supervision by

ANDREW P. VITALE

entitled

NEAR-SURFACE AIR TEMPERATURE IN COMPLEX TERRAIN: DAILY

PREDICTIONS OF FINE-SCALE (30 M) TEMPERATURE IN THE SNAKE

RANGE, NEVADA, USA

be accepted in partial fulfillment of the
requirements for the degree of

MASTER OF SCIENCE

Thomas P. Albright, Ph.D. – Advisor

Stephanie A. McAfee, Ph.D. – Committee Member

Peter J. Weisberg, Ph.D. – Graduate School Representative

David Zeh, Ph.D. – Dean, Graduate School

May 2015

ABSTRACT

Air temperature is arguably the most important component of the mountain climate, and scientists have been studying it for centuries. Recently, researchers have used arrays of inexpensive temperature sensors to observe and understand temperature across the landscape. Much of this work has focused on landscape scale features as drivers of local air temperature's divergence from the greater regional air mass. To this end, we conducted an empirical orthogonal function analysis of gridded sea level pressure (SLP) from 1951-2014 for a spatial window including the eastern Pacific and western North America, which identified a mode of SLP variability that well describes synoptic weather in our study area. Pressure patterns and NCEP Reanalysis 1 derived regional air temperature were linked with a network of 40 temperature sensors spanning June 2013-2014 and GIS derived landscape variables to create hierarchical-mixed effects models of daily minimum and maximum temperature in the Snake Range. Minimum temperatures were mostly linked to elevation and the shape of the landscape, as cold air drainage is a common process in the Snake Range. Maximum temperature was largely related to insolation and elevation, with a large seasonal component. We used these models to create maps coinciding with daily Snake Range Sensor Network readings of minimum and maximum temperature in the Snake Range at 30 m spatial resolution. The map predictions were validated using an independent dataset and a leave-one-out cross validation. Overall mean absolute error for minimum and maximum temperature were 1.92 and 2.78 °C when calculated with the independent dataset and 1.84 and 2.21 °C when calculated using the leave-one-out cross validation. Together, these results show that temperature regimes in complex terrain vary considerably over short distances and short periods of time. It is possible to create a more realistic representation of maximum and minimum temperature

for a particular study area, and the topoclimate of maximum and minimum temperature identified here can likely be applied to similar systems.

DEDICATION:

I dedicate this thesis to my family, who have shown me unwavering support and

patience throughout my life.

To Mary, James, Alexander, and Nicole Vitale.

ACKNOWLEDGEMENTS

regards to instrumentation. A giant thanks to Denis Mutiibwa, Keeley Rideout, and Sarah Hardage for their innumerable assistance in the field and in the construction of over 80 radiation shields! Thanks to David Simeral for his thoughts on instrumentation in the mountains. Also a big thanks to Zachary Holden for sharing his experiences with similar research in Idaho and for sharing a how-to video on building inexpensive radiation shields, all of which has taken place without ever meeting face-to-face! A quality education can only take place in an environment that encourages learning and with a group that desires new knowledge, so I would like to show my appreciation to the entirety of the UNR Department of Geography. The faculty and my fellow students here have contributed to my growth throughout the years.

TABLE OF CONTENTS

1   Near-Surface Air Temperature in Complex Terrain: Daily Predictions of Fine-Scale (30 m) Temperature in the Snake Range, Nevada, USA   **1**

Appendices   **53**

A Hierarchical Mixed-Effects Model Fitting   **53**

LIST OF TABLES

LIST OF FIGURES

CHAPTER 1

NEAR-SURFACE AIR TEMPERATURE IN COMPLEX TERRAIN: DAILY

PREDICTIONS OF FINE-SCALE (30 M) TEMPERATURE IN THE SNAKE

RANGE, NEVADA, USA

1.1   Introduction

Air temperature is an essential component of climate in mountainous areas (Lookingbill and Urban, 2003; Barry, 2008). It affects many parts of the mountain system such as the timing of snow melt, evapotranspiration, photosynthesis, drought tolerance, carbon fixation, and the distribution of plants and animals (Cabrera et al., 1998; Barry, 2008; Adams et al., 2009; Geiger et al., 2009; Crimmins et al., 2011). Near-surface air temperature is frequently a focal point of climate change impact studies and resource management alike (Diaz et al., 2003; Millar et al., 2007), highlighting the importance of understanding and accurately representing this dynamic environmental parameter across the landscape.

Near-surface air temperature gradients tend to vary over short distances and with the seasons in mountain settings, making for a complex spatio-temporal pattern. Patterns of near-surface air temperature are driven by both regional and landscape-scale characteristics (Steinhauser, 1967; Dobrowski et al., 2009). In the context of this work, regional-scale characteristics refers to synoptic-scale weather patterns and larger-scale geographic features such as the orientation of mountain ranges, latitude, and distance to significant water bodies. Landscape-scale characteristics refers to site specific conditions at the scale of the watershed (Dobrowski et al., 2009). While elevation is often highly correlated with surface air temperature (temperature decreases with increasing elevation), this relationship alone does not

account for the variation of temperature in mountain environments, as fine-scale variations in net solar radiation occur due to varying landscape-scale characteristics such as the terrain slope and orientation, shading from local vegetation, and variation in evapotranspiration across the landscape, which can have profound effects on surface air temperature (Geiger et al., 2009; Barry, 2008; Dobrowski, 2011; Fridley, 2009; Lundquist and Cayan, 2007). The influence of these landscape-scale characteristics is dynamic through time, changing with the seasons and synoptic weather conditions.

While the need to understand near-surface air temperature in mountain environments is clear, it has proven very difficult to accurately estimate temperature patterns in complex terrain. A common method of estimation has been the use of a lapse rate of -6.5 °C km^{-1} (e.g. Martinec and Rango, 1986). This method describes an average that fails to account for spatial differences in temperature driven by topography, humidity, substrate, and many other factors (Barry, 2008; Geiger et al., 2009), most of which vary greatly at different locations. Moreover, the use of a standard lapse rate fails to account for temporal variation in the relationship between elevation and near-surface air temperature, which is known to vary greatly on both diurnal and seasonal time scales, particularly in arid mountain settings. Lapse rates tend to be steeper during the day than at night, and they also tend to exhibit seasonal variations, with steeper lapse rates during the warmer months than the colder months (Barry, 2008; Rolland, 2003; Pepin et al., 1999).

Synoptic weather also plays a large role in the variation of near-surface air temperature in mountain environments. Although Blandford et al. (2008) found few seasonal differences in lapse rates, they showed that lapse rates for daily maximum temperature (T_{max}) and daily minimum temperatures (T_{min}) varied with synoptic

conditions in the mountains of south-central Idaho. However, they found the relationship with T_{max} lapse rates and synoptic conditions was more tenuous than that of T_{min} lapse rates. Their study showed that lapse rates were generally steeper while warmer air masses were present and more shallow when dry air masses prevailed. They found that the largest diurnal fluctuations in lapse rates occurred during dry tropical air masses, largely due to the clear skies associated with these synoptic conditions.

Another study conducted by Pepin et al. (1999) found that synoptic conditions also have a large effect on lapse rates in northern England, with anticyclones leading to larger differences between T_{max} and T_{min} lapse rates. Anticyclones are generally associated with calm weather and clear sky conditions. Calm conditions and clear skies typically lead to cold air drainage during nighttime minima due to the escape of long wave radiation since there is no cloud cover to trap the radiation. Radiative cooling of the near-surface air through conduction with the ground surface occurs, and the more dense air naturally sinks down the slope of the mountain leading to lower temperatures at the valley floor than at higher elevations. Conversely, T_{max} lapse rates tend to increase under these conditions, as more short wave radiation reaches the ground surface under clear skies which leads to a well mixed near-surface atmosphere (or boundary layer) due to convection.

Methods other than lapse rates have been developed to estimate near-surface air temperature, particularly in the form of gridded datasets based on station observations. Three popular examples of such gridded datasets are PRISM, Daymet, and WorldClim (Daly et al., 2008; Thornton et al., 1997; Hijmans et al., 2005). These three examples all attempt to account for spatial variation in temperature. PRISM uses a climate-elevation regression to account for variations in lapse rates through-

out the continental United States. The model weights each individual station based on the similarity of the station's topography to that of a digital elevation model (DEM) grid cell. PRISM also incorporates climatic data about the upper atmosphere in an attempt to better model complicated situations such as inversion layers, and also relies on a "spatial climate knowledge" that has been developed over the years (Daly et al., 2008). Daymet uses a slightly different approach to create their gridded meteorological variables. The algorithm relies on the spatial convolution of a truncated Gaussian weighting filter, applying weights to different stations. Areas that have more dense observation networks tend to use a smaller station search radius, while areas with less dense observation networks (e.g. Great Basin National Park) tend to have a greater search radius. Daymet also allows for the creation of spatially averaged regression slopes (akin to spatially averaged lapse rates). The values employed by the algorithm vary greatly throughout the seasons, and are based on Thornton et al. (1997). The WorldClim dataset is another gridded climate dataset, and it is created using the thin-plate smoothing spline algorithm implemented in the ANUSPLIN package. The interpolated product relies on elevation, latitude, and longitude as independent variables to predict temperature. Much like a regression analysis, the prediction will not necessarily match the data point (Hijmans et al., 2005). WorldClim has global coverage, while PRISM and Daymet are only available for the continental United States.

While the available gridded products are useful for many applications, their use in mountainous, landscape-scale study areas is limited by their weather station inputs. Weather stations are sparse in mountain environments; thus most weather station observations come from valley locations (Hijmans et al., 2005; Myrick and Horel, 2008; Horel and Dong, 2010). The limited sampling in mountain ranges fails to quantifiably observe topographically driven temperature regimes at the

landscape-scale, hence limiting our understanding of temperature's relationship with many processes (Lundquist and Cayan, 2007; Barry, 2008; Geiger et al., 2009; Crimmins et al., 2011; Ashcroft et al., 2012).

There have been numerous efforts to characterize temperature at scales that more completely account for landscape-scale drivers of near-surface air temperature (Lookingbill and Urban, 2003; Lundquist and Cayan, 2007; Fridley, 2009; Holden et al., 2011b; Ashcroft and Gollan, 2011). These studies have employed different methods to analyze networks of temperature sensors in mountainous environments, and they share both similarities and differences in their findings. Lundquist and Cayan (2007) and Holden et al. (2011b) found that synoptic conditions were important drivers of near-surface air temperature in the Sierra Nevada of California and two mountain ranges in northern Idaho, respectively. Lookingbill and Urban (2003) and Fridley (2009) found significant effects of distance to streams on near-surface air temperatures, while Holden et al. (2011b), Ashcroft and Gollan (2011), and Lundquist and Cayan (2007) did not report investigating this variable. In general, researchers have had success in characterizing and mapping near-surface air temperatures at their respective study locations, highlighting similarities and differences in the drivers of near-surface air temperature at different locations across the globe when considering the landcape-scale. One difficulty in comparing existing landscape-scale near-surface air temperature studies is the difference in both study design (e.g. sensor height above ground, sampling locations, etc.) and statistical methods used. Thus, further study in new locations is warranted.

The goals of this study were to: (1) observe and describe how near-surface air temperature (2 m above the ground surface) varies both spatially and temporally

in a topographically complex landscape characteristic of Great Basin mountain ranges; (2) quantify the effects of synoptic weather conditions on spatial variation in near-surface air temperature; (3) demonstrate the ability to construct inferential and predictive statistical models of site-specific near-surface T_{max} and T_{min}. To achieve these goals, we have deployed the Snake Range Sensor Network (SRSN) (Figure 1.1), a network of 40 temperature sensors, in and around Great Basin National Park, Nevada, and obtained daily T_{max} and T_{min} from the sensors for the period 17 June 2013 to 24 June 2014 (totalling 373 days). We have used methods similar to Fridley (2009) by creating multilevel, mixed-effect linear models based on maximum likelihood, as these models provide the flexibility of describing hierarchically structured landscape processes while accounting for spatio-temporal autocorrelation. The model coefficients were interpreted to obtain a better understanding of how near-surface air temperature varies in the study site. We validated the hierarchical mixed effects models using two methods: (1) an independent dataset from the Nevada Climate-ecohydrological Assessment Network (NevCAN) (http://www.sensor.nevada.edu); (2) a leave-one-out cross validation approach, and finally, we produced fine scale maps (30 m resolution) of daily T_{max} and T_{min} for the study site and period using a GIS framework.

1.2 Methods

1.2.1 Study Site

Our study site (Figure 1.1) is located near and within Great Basin National Park (GBNP), Nevada, USA on the west slope of the Snake Range of eastern Nevada.
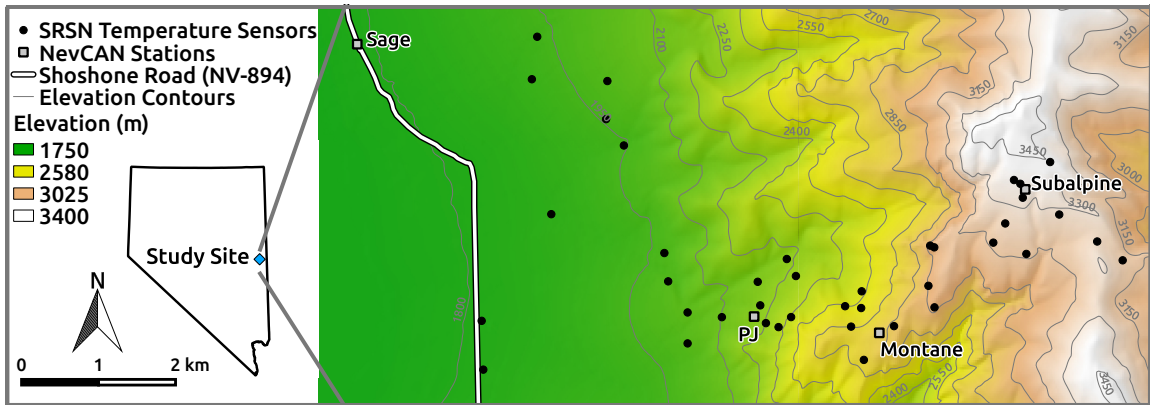
Figure 1.1: A map of the study site in the Snake Range, Nevada, USA. The blue diamond indicates the location of this study within the state of Nevada. The Snake Range Sensor Network (SRSN) locations are shown as black points on the map and the NevCAN weather stations are indicated by the gray squares and labeled by name. Colored shading indicates elevation, the gray lines are elevation contours spaced at 150 m, and the white line represents Shoshone Road (NV-894).

Typical of the Great Basin, our study site consists of a long, broad, north-south oriented valley with steep mountains to both the east and west. The average elevation of the valley is approximately 1500 m above mean sea level (AMSL), while the highest point in our study site, Mount Washington, is about 3550 m AMSL. Our study site encompasses four weather stations (Sage, PJ, Montane, Subalpine) (Figure 1.1), which are a part of NevCAN. These stations are all sited within different dominant vegetation types. From west to east, the Snake Range study site includes the sagebrush zone (dominant species: *Artemesia tridentata*), the Pinyon-Juniper zone (dominant species: *Pinus monophylla*, *Juniperus osteosperma*), the montane zone (dominant species: *Abies concolor*, *Pinus flexilis*), and the subalpine zone (dominant species: *Pinus longaeva*, *Pinus flexilis*). Approximately 10% of the study site near the subalpine zone has burned within the last 15 years. Precipitation in the area is mostly dominated by Pacific frontal storm systems in the winter, but isolated to scattered thunderstorms are also common in the summer. The annual

lapse rate for the area was calculated as -5.9 °C km^{-1} +/- 0.5 °C for the 2012 water year (1 October 2011 to 30 September 2012) (Mensing et al., 2013), thus our study site approximates the standard environmental lapse rate of -6.5 °C.

1.2.2   Snake Range Sensor Network

We installed the Snake Range Sensor Network (SRSN), a network of 40 LogTag Trix 16 temperature sensors along an elevational gradient on the west slope of the Snake Range. The sensors are housed in inexpensive radiation shields constructed of easily sourced materials which perform in a manner similar to an unaspirated Gill shield, as outlined by Holden et al. (2013). The sensors were placed 2 m above the ground surface, affixed to trees when available (in a manner similar to Lundquist and Cayan (2007); Lundquist and Huggett (2008)) and attached to PVC poles that are strapped to shrubs when no trees were nearby. It is likely that affixing the temperature sensors to trees has an effect on the temperature reading (e.g. Hough, 1945), thus there is additional uncertainty surrounding the accuracy of these measurements.

Using a GIS analysis, we identified a sampling design that diversified the topographic position and tocopoclimatic conditions sampled. The analysis consisted of splitting the mountain into four elevation zones (1500-2000 m; 2000-2500 m; 2500-3000 m; 3000-3500 m). For each elevation zone, we conducted a classification analysis using an isodata algorithm (ESRI, 2014) to identify 10 distinct clusters of data based on slope, slope position, heat load index (McCune and Keon, 2002), and the National Land Cover Dataset (NLCD) 2006 canopy cover dataset (Fry et al., 2011). This left a total of 40 unique clusters (10 clusters in each of the 4 elevation zones).

Each cluster had numerous occurrences throughout the analysis domain. To determine the final sensor location, we generated spatially random points within the 40 polygons that encompassed the largest surface area of the 40 clusters, as the largest surface area polygon is most likely to represent the combination of the input data that the Isocluster algorithm identified (Figure 1.1).

1.2.3 Predictor Variables: Synoptic Weather

Sea Level Pressure: Empirical Orthogonal Functions

It is known that synoptic weather patterns have a great influence on near-surface air temperature in areas of complex terrain (e.g. Lundquist and Cayan, 2007). In our eastern Nevada study site, both T_{max} and T_{min} can become cooler along the lower elevation valley floor than at the summit of Mount Washington. These temperature inversions occur more commonly in the Snake Range during anticyclonic patterns. Inversions tend to form due to radiative cooling of the ground surface, which in turn cools the air. The more dense, cooler air then sinks to lower elevation, concave terrain features, like the long, broad valleys of the Great Basin. Conversely, cyclonic conditions lead to a greater mixing of the boundary layer with the free atmosphere, thus a linear decrease of temperature with increasing elevation is typically observed under cyclonic conditions. Local scale topography is thought to have a greater influence on T_{min}, while T_{max} is more influenced by synoptic scale atmospheric conditions (Lundquist et al., 2008; Lundquist and Cayan, 2007; Pepin et al., 2011).

There is a long history of using empirical orthogonal functions (EOFs), also

commonly referred to as principal components analysis (PCA), to better understand two dimensional fields of meteorological data (Hannachi et al., 2007). EOFs work to decompose a dataset, a space-by-time matrix in the case of meteorological fields, into new variables. The new variables are orthogonal to one another (i.e. uncorrelated) account for much of the variance in the original data, and will be linear combinations of the original data (Hannachi et al., 2007).

Based on the variation in lapse rates and near-surface air temperature that have been related to synoptic weather conditions in our study site and locations with similarly complex terrain (Lundquist and Cayan, 2007; Lundquist et al., 2008; Blandford et al., 2008; Pepin et al., 2011), we suspected synoptic conditions would have a strong effect on both T_{max} and T_{min} in the area of the SRSN. To better understand synoptic weather in our study site, we retrieved daily average sea level pressure (SLP) grids (2.5° resolution) from the NCEP/NCAR Reanalysis 1 (Kalnay et al., 1996) for the period of 1 January 1958 to 24 September 2014 in the spatial domain of approximately 176°W to 98°W and 16°N to 68°N. Using the raster package in R (Hijmans, 2014; R Core Team, 2014), we first projected the data from a geographic coordinate system (longitude/latitude) to a planar equidistant projection using a bilinear interpolation, which accounts for the decreasing surface area of longitude/latitude grid cells at higher latitudes. We then calculated SLP anomalies on the re-gridded dataset by subtracting the mean for the entire period from each day's assimilation. EOFs, or maps displaying modes of SLP variation identified by the analysis, and their associated temporal variation (principal components or PCs) were calculated for the entire period using the spacetime package (Pebesma, 2012; Bivand et al., 2013) in R (R Core Team, 2014) (Figure 1.2 and Figure 1.3, respectively).
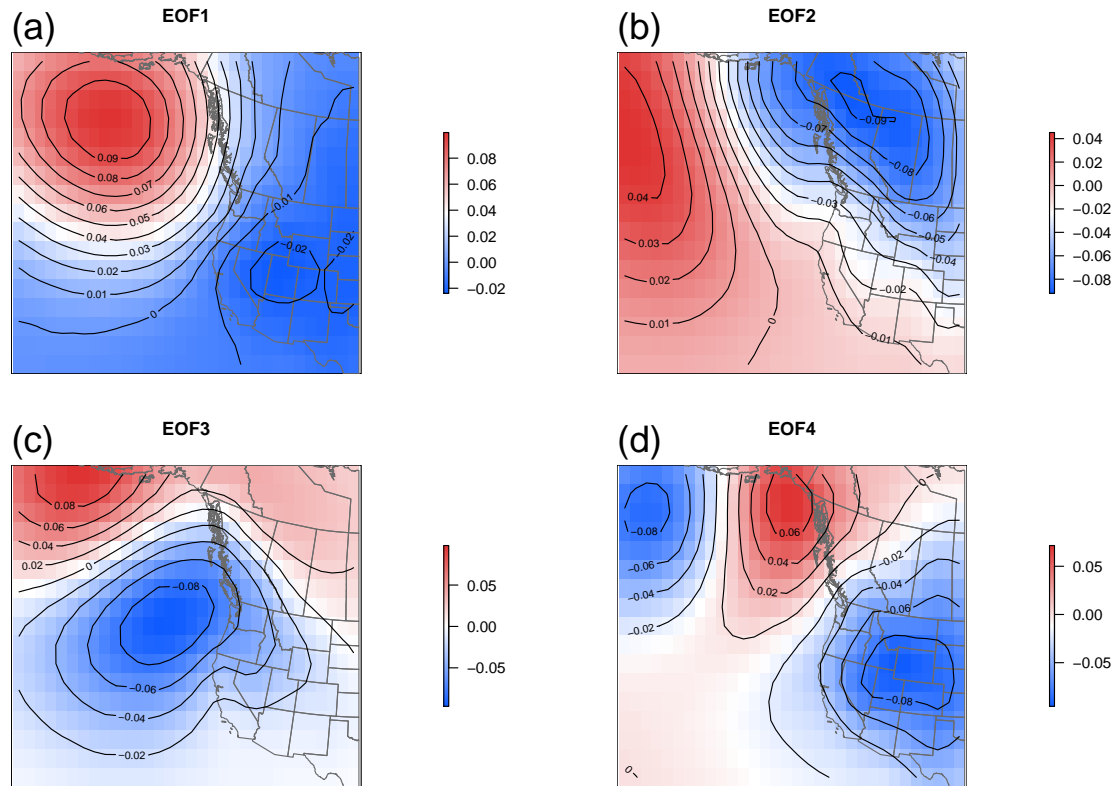
Figure 1.2: The first 4 of 544 empirical orthogonal functions (EOFs) identified by an empirical orthogonal function analysis of daily mean sea level pressure (SLP) anomalies. Physical interpretation is in the text. The variation of these spatial patterns through time as Principal Components (PCs) can be observed in Figure 1.3, where the numeric label of each PC corresponds to the numeric label of these EOFs. The percent variance explained by EOF 1, EOF 2, EOF 3, and EOF 4 are 36%, 22%, 10%, and 8% respectively (Table 1.1).

The most difficult portion of an EOF analysis is surely the interpretation. With careful consideration of both the EOFs (Figure 1.2) and their associated PC time series (Figure 1.3), we were able to identify interpretable modes of variability within SLP fields over the Eastern Pacific Ocean and the Western United States. One familiar pattern of SLP that is apparent in EOF 1 (Figure 1.2 (a)) is the Aleutian Low. This EOF accounts for 36% of the variance in SLP anomalies (Table 1.1), and displays a highly seasonal trend with negative PC values in the winter, and positive PC values in the summer (Figure 1.3 (a)).
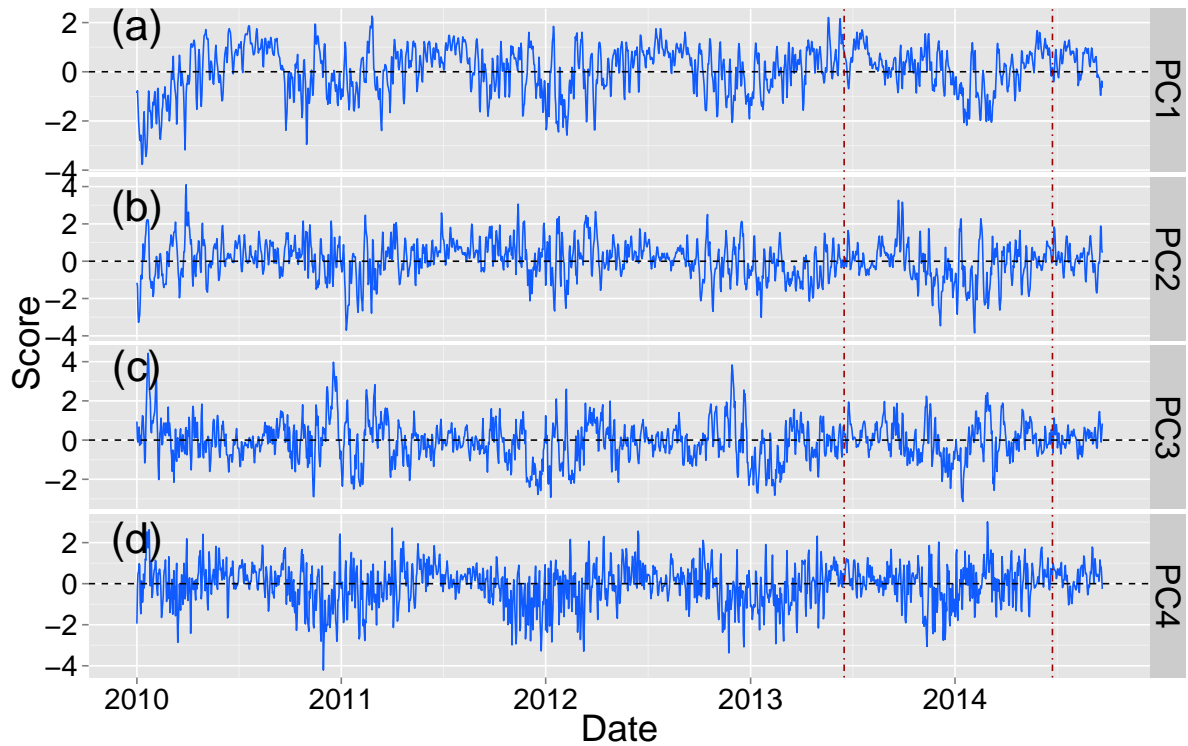
Figure 1.3: The first 4 of 544 principal components (PCs) identified and described in text. A temporal subset spanning 1 January 2009 to the final day of the analysis period, 24 September 2014, is displayed for clarity. Also note the differing y-axes, as the PC scores are relative. The vertical red lines indicate the portion of the time series that coincides with the SRSN analysis period.

Table 1.1: Summary statistics for the EOF analysis conducted on SLP anomolies for the years 1958-2014. Only the first 4 of 544 EOFs are shown.

	EOF1	EOF2	EOF3	EOF4
Standard Deviation	120.14	92.90	63.92	54.60
Proportion of Variance	0.36	0.22	0.10	0.08
Cumulative Proportion of Variance	0.36	0.58	0.68	0.76

The second EOF (Figure 1.2 (b)) represents anomalously high SLP over the Pacific and anomalously low SLP over the northeastern portion of the analysis domain. It is associated with the formation and movement of large frontal storms from the Pacific over the northern portion of the domain, while the inverse of this pattern is associated with the formation of a high pressure ridge off the coast of Western North America. Again, this EOF displays more variation during the winter season (Figure 1.3 (b)) and a largely seasonal pattern. We found that EOF2/PC2 accounts for 22% of the variation observed in SLP anomalies (Table 1.1).

The third EOF (Figure 1.2 (c)) accounts for less of the variation in SLP anomalies at 10% (Table 1.1). The pattern identified here reflects anomalously low SLP off the coast of the Western United States, and when in the negative phase, an anomalously high SLP occurs off the coast of the Western United States. While there is a fair amount of intra-annual variability of this pattern (Figure 1.3 (c)), it appears to evolve on a timescale measured in weeks rather than days.

Finally, the fourth EOF presented here (Figure 1.2 (d)) accounts for 8% (Table 1.1) of the total variance in SLP anomalies in the study domain. While not quantified, we noted that pattern displays a strong correlation with the formation and passage of low pressure systems over the western portion of the United States. This correlation was determined by inspecting a number of weather maps during periods of relatively extreme EOF 4 values (example maps in Figure 1.4). It is predominantly associated with positive values of PC 4, which exhibits daily variation in its magnitude and sign (Figure 1.3 (d)). This mode of SLP identified by the EOF analysis is indicative of changes in synoptic weather patterns on a time scale that is directly comparable to variations in daily near-surface air temperature. As a first-order test of this assertion, we calculated daily lapse rates for T_{min} and T_{max}
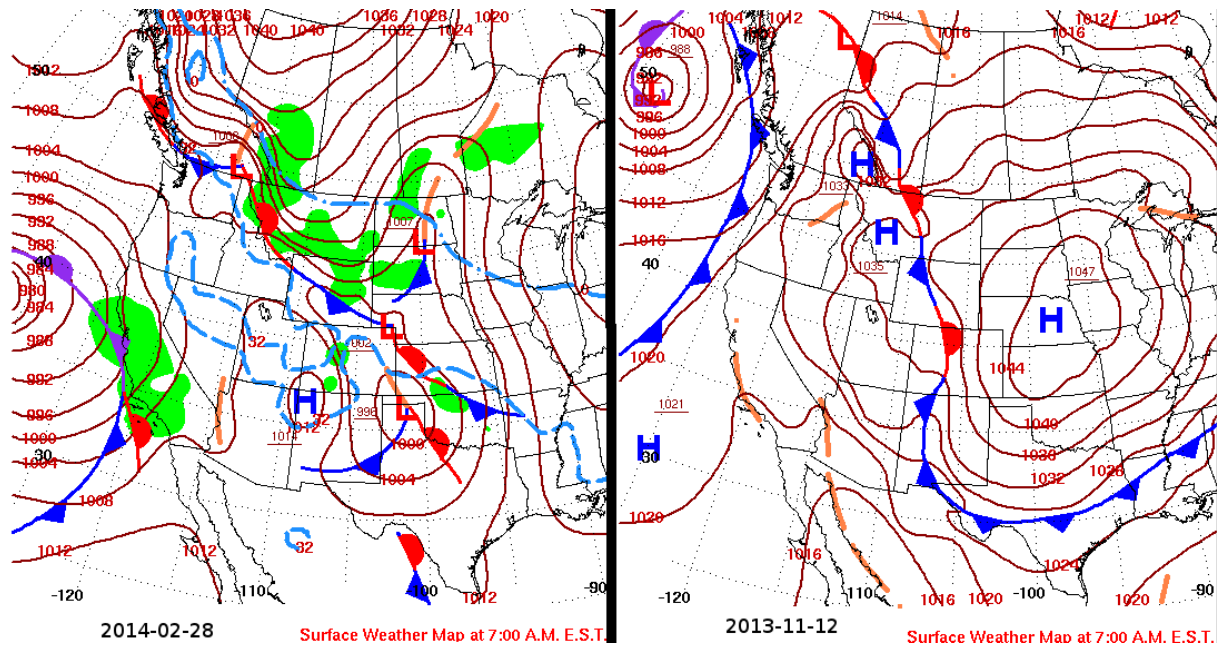
Figure 1.4: The left panel shows surface weather conditions for the study domain during 28 February 2014, a day with a relatively high value of PC4 and the presence of a relatively unstable air mass (Figure 1.3). The right panel shows surface weather for 12 November 2013, a day with relatively low values in PC4 and a high pressure system dominating the study domain. Maps from http://www.hpc.ncep.noaa.gov/dailywxmap/.

from the SRSN data. The Pearson's Correlation Coefficient of lapse rates and PC4 were calculated as -0.40 for T_{max} and -0.41 for T_{min}. Thus, we considered PC4 as a predictor variable in our hierarchical mixed-effects models for near-surface air temperature at the study site in an attempt to quantify the effects of synoptic scale circulations on temperature patterns in the region.

Free Air Temperature

As one of the underlying interests of this study is characterizing terrain's ability to create local deviations in temperature from the free-air, we need an effective means of representing free-air temperature for our study site. Our study site lies

within a single grid cell of the NCEP/NCAR Reanalysis 1 (Kalnay et al., 1996). The Reanalysis 1 project assimilates data from a number of sources, including land, ship, satellite, radiosondes, and others, using an operational weather forecasting model to interpolate the data. Assimilations are produced 4-times daily and include daily and monthly means. We use daily mean air temperature at the 700 hPa level to indicate free-air temperature at our study site, as this pressure level is generally found at approximately 3000 m AMSL. The exact height AMSL of the 700 hPa level varies on a daily basis. We have extracted a time series of daily average temperature from the 700 hPa level for the period 17 June 2013 to 24 June 2014, which we use to indicate regional air mass temperature (Figure 1.5). Temperature at 700 hPa is expected to be generally cooler than the near-surface air temperature. Additionally, it is highly correlated with daily T_{min} and T_{max} (r = 0.92 and 0.84 respectively).

Seasonality

There is a large component of seasonality that affects regional air mass temperature and which topographic variables have the greatest influence over temperature across the landscape. While we make an attempt to quantify the two most notable effects of seasonality (regional air temperature and low pressure systems), we acknowledge that limitations of data and understanding of the system prevent quantifying every individual seasonal effect (e.g. the depth and spatial distribution of snow). Such maps detailed enough for inclusion in a landscape-scale topoclimate study do not exist for the study site or period. To this end, we have included a sine and cosine wave for consideration as predictor variables. The values of these variables are calculated as $cos(2\pi/365 \times JDAY)$ or $sin(2\pi/365 \times JDAY)$ where JDAY
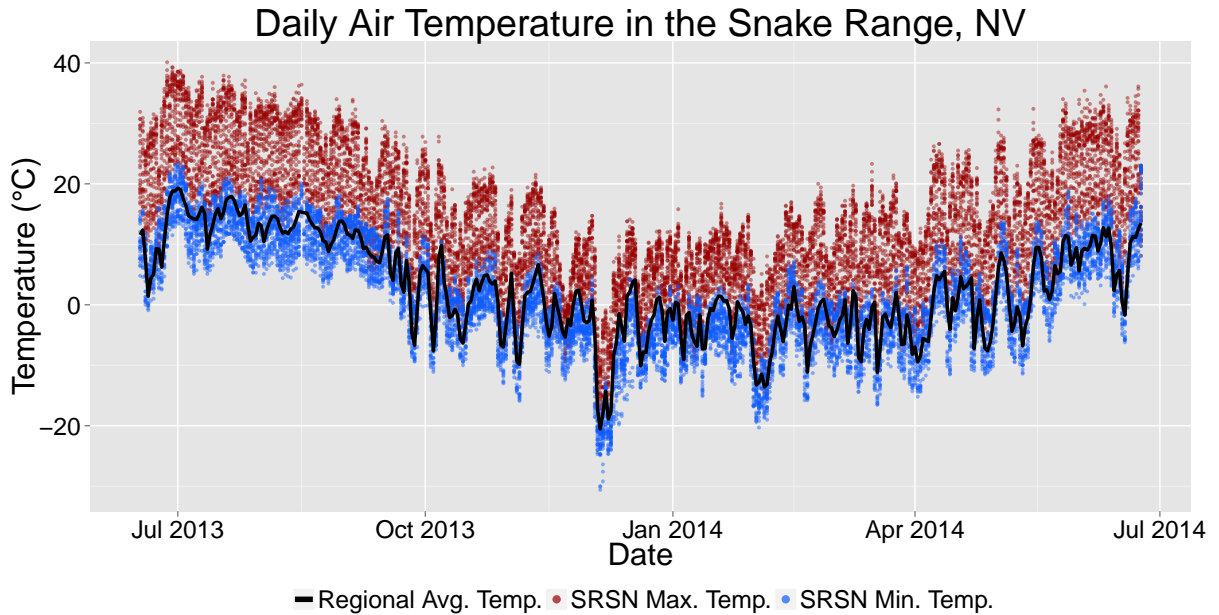
Figure 1.5: A time series showing all SRSN maximum and minimum daily temperature data collected during the study period (17 June 2013 to 24 June 2014) as semitransparent red and blue symbols, respectively, and the NCEP Reanalysis 1 daily average air temperature at the 700 hPa level drawn as a black line. All of the SRSN T_{max} and T_{min} data are plotted for each day, thus up to 80 dots are present on each day. Due to the data points being drawn as semitransparent, darker shades of red and blue indicate greater point density on the scatterplot.

is the day of year as an integer (1-365 on non-leap years) and $2\pi/365$ indicates a full annual cycle.

1.2.4   Predictor Variables: Topography

A number of studies have successfully associated processes that drive landscape-scale near-surface air temperature with easily measured features of the landscape (e.g. elevation, slope, topographic position indices) (Fridley, 2009; Dobrowski et al., 2009; Ashcroft and Gollan, 2011). Here, we present a brief description of the main landscape feature we expect to contribute to T_{min} and T_{max} at our study

site.

For a given geographic location and time, maximum temperatures tend to vary based on the amount of direct beam solar radiation that is received at the location (Geiger et al., 2009). This is mostly controlled by the slope and aspect of the surface in complex terrain, with additional influences due to shading caused by adjacent topographic features. The radiation warms up the land surface, which in turn acts to warm the near-surface air (Geiger et al., 2009).

Minimum temperatures are indirectly related to daily solar energy balances, but are influenced more directly by the movement of cold air over the landscape (e.g. katabatic winds and cold air drainage). The loss of longwave radiation from the ground surface is an important process for T_{min}, and is largely determined by slope angle and vegetation cover (Fridley, 2009; Geiger et al., 2009).

For our study site, we suspected that the principal landscape-scale drivers of near-surface air temperature are incoming solar radiation, cold air drainage (more commonly in T_{min} than T_{max}), and evapotranspiration. GRASS GIS 6.4 (GRASS Development Team, 2012) has implemented the r.sun algorithm, which calculates direct beam, diffuse, and reflected radiation for a given raster cell on a given day from an input DEM. It considers latitude, shading from nearby terrain features, day of year, slope orientation, and slope angle in its estimate of solar irradiance (Wm^2). A preliminary analysis was conducted using a similar metric, the heat load index (McCune and Keon, 2002), but early indications pointed towards the GRASS r.sun algorithm as a superior method for estimating clear-sky solar irradiance.

As expected, the large range of elevations exhibited in our study site are associated with a rapidly changing vegetation structure as you travel east to west across

the study site (Figure 1.1). Vegetation cover tends to have a moderating effect on near-surface air temperature. Areas of high canopy cover tend to stay slightly warmer at night and slightly cooler during the day, making canopy cover a large component of the near-surface energy balance. We have downloaded the 2011 United States Geological Survey (USGS) National Landcover Database (NLCD), a remotely sensed product that includes an estimate of percent canopy cover at 30 m resolution for the conterminous United States (Jin et al., 2013), for consideration as predictor variables in our T_{min} and T_{max} models.

Cold air drainage has been represented by the terrain convergence index (TCI), which can also be easily calculated in GRASS GIS (r.terraflow algorithm). This algorithm calculates the accumulation of a fluid over terrain, requiring only a DEM as input. TCI at our study site ranged in values from 2.1-17.1, where higher values are associated concave terrain features. As cold, dense air tends to respond similarly to water, we anticipate areas of high TCI values are more likely to encounter cold air drainage. Dobrowski et al. (2009) successfully used TCI as a proxy to cold air drainage.

The slope angle of the terrain can also play a major role in the near-surface energy balance. Terrain slope can act as a further proxy to cold air drainage, as low slope areas are more likely to experience accumulation of cold air. Further, slope is also influential in the amount of solar irradiance received at an area. We have included terrain slope as a variable for consideration. All terrain variables were derived in GIS software using an approximately 30 m resolution DEM obtained from the USGS.

1.2.5 Model Construction

Similar to Fridley (2009), we used a mixed-effects hierarchical linear model structure to predict T_{min} and T_{max} from synoptic weather conditions and GIS derived predictor variables. These models are effective at representing nested data, as they incorporate both fixed effects and random effects. Fixed effects are measurable environmental variables, while random effects are unmeasured noise associated with individual samples or groups of samples (Pinheiro and Bates, 2000). Given the serial correlation of temperature within our study site through both space and time, mixed effect models are further justified, as they provide the benefit of describing nested covariance structures. In the case of our study, temporal variation is nested within each spatial location (i.e. each sensor location as seen in Figure 1.1). The sampling design of this study results in a model of two nested levels. The first level is the daily variation of temperature at each site. We have observed T_{max} and T_{min} over the course of 373 days (17 June 2013 to 24 June 2014). The second level of the model describes variation across space (i.e. the mean temperature over the 373 days of observations varies as a function of spatial location on the landscape). The mixed-effects hierarchical linear model structure allows for random effects to be associated with each sample unit (here days within location and each individual location). The random effects describe variance in the response that can not be attributed to the environmental variables included within the model (i.e. the fixed effects), thus can account for noise that would affect model extrapolation to the landscape.

A detailed list of the predictor variables used in the modeling is included as Table 1.2. The final T_{max} and T_{min} models were selected using a forward fitting procedure. We started with relatively simple models that included key topographic and

landscape variables, such as elevation, TCI, and NLCD canopy cover. Additional independent variables were added to the models based on physical relevance and interpretability. We used Aikake's information criterion (AIC) to determine if each additional model term improved the fit of the model to the data until we reached a model that is statistically robust and physically relevant. Second order interactions and polynomials were considered for all variables, but were only tested for model inclusion using AIC when a physically relevant explanation could be provided. Much of the spatial and temporal autocorrelation is addressed by inclusion of random effects in the final models. Models were fit with and without an exponentially decaying temporal covariance structure, but the added complexity did not improve fit as indicated by log likelihood tests and AIC. As the relationship between elevation and T_{min} and T_{max} change daily, the inclusion of a random slope for elevation and its quadratic were tested using AIC. The tests indicated that random slopes by elevation improved the model fit, thus these terms were included in both final models. A more detailed description of the model fitting procedure and the final fitted models is described in Appendix A. We fit the models with R version 3.1.2 (R Core Team, 2014). Both the "nlme" (Pinheiro et al., 2014) package and the "lme4" (Bates et al., 2014) package were used to fit the hierarchical models.

Table 1.2: Predictor variables used both the minimum and maximum daily temperature models that are described in text. The variable name, a brief description of the variable, the units of the variable, range of observed values, and data source are included in this table.

Variable	Description	Units	Range of Values	Source
T_{air}	Daily mean temperature at 700 hPa	°C	-20.55 - 19.27	NCEP Reanalysis 1
PC4	Daily fluctuations of SLP		-4.96 - 4.70	EOF Analysis of daily SLP
ELEV	Elevation (AMSL)	km	1.56 - 3.85	USGS elevation model
TCI	Terrain Convergence Index		2.1 - 17.1	r.terraflow in GRASS GIS
IRRAD	Daily shortwave radiation	MWm^2	0.378 - 9.81	r.sun in GRASS GIS
CC	Canopy Cover	%	0 - 72	USGS NLCD 2011
SLOPE	Terrain Slope	°	0 - 73.3	GIS derived from elevation
JDAY	Day of year		1 - 365	Gregorian Calendar

1.2.6 Model Validation and Mapping

Model Validation with an Independent Dataset

To validate our models of T_{max} and T_{min} for the entirety of the mapped region, we downloaded daily maximum and minimum temperature at 2 m above the ground surface from the NevCAN stations in the region (Sagebrush, PJ, Montane, Sub-alpine; Figure 1.1). The models were used to predict T_{max} and T_{min} for these locations, and we calculated model bias (difference between predicted and observed temperature, Table 1.3), accuracy (mean absolute error [MAE], calculated as the difference between the predicted and observed temperature after all values have been made positive, Table 1.4), and root mean squared error ([RMSE], calculated as the square root of the mean bias squared, Table 1.5).

Table 1.3: Model bias for daily maximum and daily minimum temperature models described in text. Bias is calculated as predicted temperature minus observed temperature. Average bias per month (Figures 1.11 and 1.12) at each NevCAN station (Figure 1.1) are displayed here as well as overall average bias for the entirety of the time series.

Site	Jun	Jul	Aug	Sep	Oct	Nov	Dec	Jan	Feb	Mar	Apr	May	Overall
Minimum Temperature Bias													
Sage	1.80	0.27	0.47	-2.24	1.24	1.33	5.56	2.47	-0.81	0.09	-0.98	0.77	0.85
PJ	2.88	1.69	1.98	-0.82	2.76	3.57	7.69	4.05	0.72	1.63	0.51	2.29	2.43
Montane	-0.54	0.07	-0.74	-0.54	-0.16	0.05	1.21	-0.33	-0.32	0.51	0.13	0.12	-0.05
Subalpine	-0.61	-0.06	-0.10	-1.14	-0.84	-0.30	-0.41	-1.70	-0.97	0.55	0.30	0.36	-0.40
Overall	0.53	0.49	0.40	-1.19	0.75	1.16	3.51	1.12	-0.34	0.70	-0.01	0.88	0.69
Maximum Temperature Bias													
Sage	-0.89	0.25	-0.35	-0.11	-1.73	0.51	3.92	-0.01	-0.73	-1.04	-0.17	0.71	0.05
PJ	-4.27	-3.14	-3.78	-3.58	-5.16	-2.82	0.64	-3.34	-4.17	-4.57	-3.67	-2.72	-3.36
Montane	-4.75	-3.10	-3.86	-2.40	-3.37	-2.33	-3.61	-3.71	-3.40	-3.00	-2.96	-2.31	-3.22
Subalpine	-3.55	-1.55	-2.36	-0.32	-1.62	-0.05	-1.83	-1.63	0.34	-0.16	-0.22	-0.22	-1.12
Overall	-3.20	-1.88	-2.59	-1.60	-2.97	-1.17	-0.22	-2.17	-1.99	-2.19	-1.75	-1.13	-1.92

Table 1.4: Model MAE for daily maximum and daily minimum temperature models described in text. MAE is calculated as the difference between the predicted and observed temperature after all vaules have been made positive. MAE at each NevCAN station (Figure 1.1) are displayed here as well as overall average bias for the entirety of the time series.

Site	Jun	Jul	Aug	Sep	Oct	Nov	Dec	Jan	Feb	Mar	Apr	May	Overall
Minimum Temperature MAE													
Sage	2.98	1.78	2.32	2.50	3.98	2.73	6.15	4.82	2.77	2.70	2.56	2.49	3.16
PJ	1.58	1.65	1.87	1.64	1.85	1.76	1.85	2.00	2.55	1.88	2.11	1.43	1.84
Montane	1.08	1.14	1.28	1.14	1.47	0.83	1.61	1.25	1.43	1.46	1.31	1.30	1.27
Subalpine	1.02	0.82	0.80	1.44	1.67	1.55	1.88	2.14	1.70	1.57	1.54	1.17	1.43
Overall	1.56	1.35	1.57	1.68	2.24	1.72	2.87	2.55	2.11	1.90	1.88	1.60	1.92
Maximum Temperature MAE													
Sage	1.90	1.35	1.33	2.23	2.53	3.14	4.68	1.95	2.48	1.86	2.03	1.75	2.27
PJ	2.86	2.14	2.47	2.84	3.19	3.04	1.81	2.32	2.47	2.54	2.96	2.40	2.59
Montane	4.64	3.47	4.04	3.45	3.73	2.94	3.70	3.71	3.69	3.50	3.80	3.38	3.69
Subalpine	3.60	2.07	2.79	2.34	2.93	2.63	2.84	2.68	2.35	2.21	2.00	2.03	2.56
Overall	3.36	2.26	2.65	2.72	3.10	2.94	3.26	2.67	2.75	2.53	2.70	2.39	2.78

Table 1.5: Model RMSE for daily maximum and daily minimum temperature models described in text. RMSE is calculated as the square root of the mean bias squared. RMSE at each NevCAN station (Figure 1.1) are displayed here as well as overall average bias for the entirety of the time series.

Site	Jun	Jul	Aug	Sep	Oct	Nov	Dec	Jan	Feb	Mar	Apr	May	Overall
Minimum Temperature RMSE													
Sage	3.72	2.23	2.89	3.06	4.56	3.35	8.00	5.76	3.56	3.22	3.13	3.05	4.18
PJ	2.04	1.90	2.33	1.99	2.28	2.01	2.25	2.60	2.96	2.41	2.54	1.93	2.28
Montane	1.40	1.49	1.51	1.41	1.86	1.11	2.21	1.63	2.00	2.29	2.09	1.65	1.75
Subalpine	1.34	1.13	1.02	1.73	1.97	1.99	2.35	2.54	2.16	2.36	2.26	1.45	1.91
Overall	2.19	1.74	2.07	2.14	2.89	2.26	4.46	3.50	2.74	2.60	2.54	2.11	2.70
Maximum Temperature RMSE													
Sage	2.55	1.76	1.79	2.81	2.90	4.11	5.64	2.52	2.95	2.20	2.55	2.52	3.04
PJ	3.35	2.54	2.74	3.41	3.54	3.66	2.16	2.76	3.24	2.93	3.32	2.81	3.07
Montane	5.06	3.94	4.35	3.82	4.05	3.34	4.03	4.05	4.32	4.05	4.22	3.86	4.13
Subalpine	3.96	2.46	3.06	2.81	3.28	3.37	3.53	3.26	2.76	2.49	2.40	2.44	3.04
Overall	3.92	2.79	3.12	3.24	3.47	3.63	4.04	3.20	3.37	3.00	3.21	2.96	3.35

Leave-One-Out Cross Validation

To further validate our models of T_{max} and T_{min}, we conducted a leave-one-out cross validation. In this procedure, we used all of the SRSN data to fit the models as described in text. Once the final models for T_{max} and T_{min} were decided, we refit the model to 39 of the 40 sensors. We used the coefficients produced by the model that was without observations from one of the SRSN sensors to predict maximum and minimum temperature values for the geographic location of the 40th sensor (i.e. the sensor that was left out). This process was repeated 40 times until all sensors had been left out. We then calculated mean square error, root mean square error, mean absolute error, and bias for all 40 model runs (Table 1.6).

To generate spatial maps of T_{max} and T_{min}, the fixed-effect coefficients of the models were then used to predict temperature for a grid with square cells of approximately 30 m for the entire study area during the entire period of observation (17 June 2013 to 24 June 2014). Maps were generated within R, using the "rgdal" (Bivand et al., 2014) and "raster" (Hijmans, 2014) packages to handle the spatial data and apply the fixed effects to the GIS predictor variables. Predicted T_{max} and T_{min} are available as GeoTIFF files.

Table 1.6: Model validation statistics for the T_{min} and T_{max} models described in text. Mean squared error (MSE) is calculated as the mean of the observed value minus the prediction squared, root mean squared error (RMSE) is the square root of MSE, mean absolute error (MAE) is calculated as the mean of the absolute value of the observation minus the predicted value, and the bias is calculated as the observed value minus the predicted value. Monthly means are calculated using leave-one-out cross validation, and the overall values are the mean value for each statistic over the course of the 373 day SRSN observations.

Statistic	Jan	Feb	Mar	Apr	May	Jun	Jul	Aug	Sep	Oct	Nov	Dec	Overall
					Minimum Temperature								
MSE	9.07	6.56	6.63	5.10	4.11	4.19	3.52	3.21	4.44	6.61	4.96	12.98	5.95
RMSE	3.01	2.56	2.58	2.26	2.03	2.05	1.88	1.79	2.11	2.57	2.23	3.60	2.39
MAE	2.33	2.05	1.92	1.72	1.60	1.60	1.49	1.38	1.64	1.99	1.75	2.64	1.84
Bias	0.16	1.15	-0.13	0.20	-0.38	0.13	-0.45	0.01	0.83	0.24	-0.14	-1.41	0.02
					Maximum Temperature								
MSE	6.32	7.54	6.05	8.22	8.34	10.62	5.24	4.05	9.64	7.44	12.28	10.42	8.01
RMSE	2.51	2.75	2.46	2.87	2.89	3.26	2.29	2.01	3.10	2.73	3.50	3.23	2.80
MAE	1.96	2.25	2.00	2.33	2.17	2.49	1.75	1.59	2.46	2.28	2.71	2.53	2.21
Bias	0.56	0.15	0.18	-0.20	-0.86	0.92	-0.32	0.24	-0.48	0.91	-0.71	-0.45	0.00

1.3   Results

1.3.1   Synoptic Patterns in the Snake Range

Large variations in average daily temperature of the free air mass (i.e. NCEP Re-analysis 1 daily average temperature at 700 hPa) were observed in the Snake Range between 17 June 2013 and 24 June 2014. The regional air mass maximum temperature value of 19.3 °C occurred on 1 July 2013, while the minimum value of -20.6 °C occurred on 5 December 2013. This minimum value is substantially lower than the majority of winter days in the region (Figure 1.5). It occurred during what can be thought of as an extreme cold event (a "cold snap") that spanned approximately 4 December 2013 to 9 December 2013. Average temperature in the region dropped from -4.9 °C to -17.3 °C in the span of 24 hours. Between 9 December 2013 and 10 December 2013 temperatures warmed in a similarly sudden manner, with average daily temperature of the regional air mass jumping from -17.7 °C to -8.4 °C in a 24 hour span. PC4 (an indicator of low pressure system passage, with positive values representing low pressure and negative values representing high pressure) shows the greatest variation in the winter months (Figure 1.3), which is consistent with the climatology of the region. Throughout our record, the cold events are typically preceded by high values of PC4. For example, the maximum value of PC4 during the period of the SRSN occurred on 28 February 2014 with a value of 3.0. This date precedes the onset of a "cold snap" in the Snake Range area (Figure 1.5), with temperatures dipping for a period of a few days. This pattern represents a cold front moving through the area. The low pressure is indicated by PC4. Once the front clears, high pressure builds with a cold air mass in place, thus persistent low temperatures occur. A local maximum of PC4 also occurs prior to the 5 Decem-
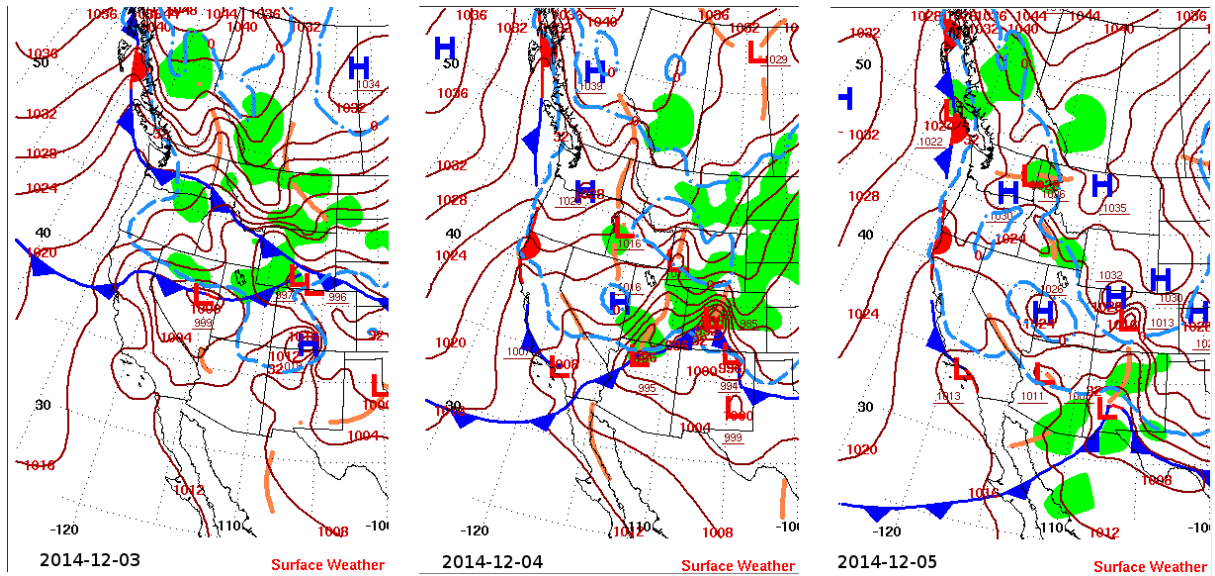
Figure 1.6: A sequence of weather maps that coincide with a "cold snap" in the Snake Range, Nevada, USA. The left most map is from 3 December 2014, the middle map is from 4 December 2014, and the right most map is from 5 December 2014. The passage of the low on 3 December 2014 is well exhibited in this sequence of maps, which are downloaded from http://www.hpc.ncep.noaa.gov/dailywxmap/index_20131203.html. Advance the maps by clicking "NEXT DAY".

ber 2013 "cold snap" (Figures 1.3 and 1.5 and the NCEP daily weather map tool (Figure 1.6)).

1.3.2   Temperature Variation across the SRSN

Minimum Temperature

There is a significant amount of temporal variation in minimum temperature across the SRSN (Figures 1.3 and 1.7). Typical of mountain environments, elevation is generally a strong predictor of temperature. However, this relationship often breaks down, and other terrain factors have a large influence over temperature at a par-

ticular location. Partial residual plots were constructed using the average monthly temperature for each sensor location. The residuals were derived from the fitting of a linear mixed-effects model of T_{min}, allowing the intercept to randomly vary by month. The residual of this model indicates variation in T_{min} that could not be explained by elevation. Comparisons of the residuals to other topographic indices were made to gain a better understanding of when and how temperature and elevation diverge. Terrain slope better explained the residuals when compared to TCI and NLCD canopy cover, as was exhibited by fitting a generalized least squares regression to predict the residuals and comparing model fits using AIC. The relationship between residual minimum temperature and slope is fairly constant throughout the course of the year, displaying larger variance at lower slope angles and a consistent relationship across months with a slightly steeper relationship in the winter months (results not shown).

Conversely, the relationship between TCI and residual minimum temperature shows large variability across months (Figure 1.7). The winter months show a strong negative relationship between residual minimum temperature and TCI, with higher values of TCI generally associated with negative T_{min} residuals. This indicates that areas with high TCI values (valley floors) are experiencing colder than expected T_{min} values when only elevation is considered. While this relationship holds true for the winter months, there does not appear to be a significant relationship in the spring, summer, or fall.

Maximum Temperature

There is a large amount of variation present in daily maximum temperature across the SRSN (Figures 1.5 and 1.8). Elevation is an even stronger predictor of maxi-
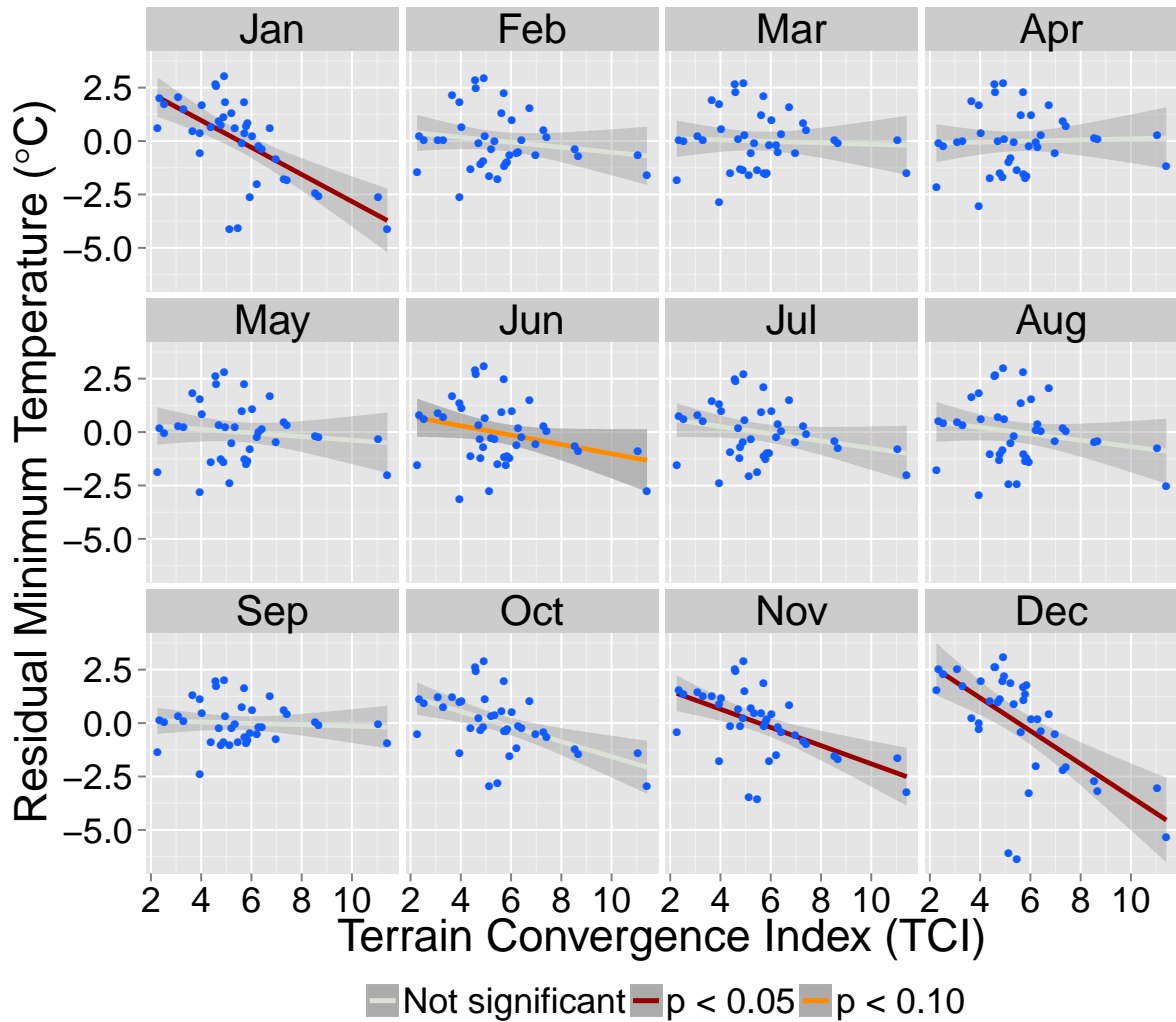
Figure 1.7: Modeled minimum daily temperature averaged over the course of a month between 17 June 2013 and 24 June 2014 expressed as a function of terrain convergence index (TCI). Temperature is expressed as the residual of a mixed- effect model fit to the entirety of the SRSN data predicted solely by elevation with random intercepts by month. Residuals are averaged for each site per month, and plotted against the TCI value at each sensor. The lines are fit by least squares regression. Lines are colored by the p-value associated with these least square regressions, where red indicates significance at the 0.05 level ($p < 0.05$), orange indicates significance at the 0.10 level ($p < 0.10$), and gray indicates no significance at the 0.10 level ($p \geq 0.10$). The gray shading associated with each regression line indicates the standard error.

mum temperature in the Snake Range than it is for minimum temperature. Partial residual plots were constructed using the residuals of a linear mixed-effects model of T_{max}, allowing the intercept to randomly vary by month, using average monthly temperature for each sensor location. Again, similar to minimum temperature, terrain slope best explained the residuals of the maximum temperature model. The strength of this relationship varies by month, with the strongest positive linear relationship occurring in the winter months, when inversions are most likely to form. The residuals of maximum temperature predicted by elevation are most variable in winter, and closest to 0 in the summer months (Figure 1.8).

1.3.3 Model Performance and Validation

Model Validation with an Independent Dataset

We calculated model bias (Figure 1.9 and Figure 1.10), mean absolute error (MAE), and root mean square (RMSE) for the maximum and minimum daily temperature hierarchical mixed-effects models (Table 1.3, Table 1.4, and Table 1.5, respectively). These tables show the performance of the T_{min} and T_{max} models for each month of the record as well as at 4 separate NevCAN sites, which are associated with different vegetation types and distinct elevations (Figure 1.1).

The T_{min} model displayed a relatively small bias when averaged over sites and months of 0.69 °C (Table 1.3). Bias was relatively low for the Sage (0.85 °C), Montane (-0.05 °C), and Subalpine sites (-0.40 °C), while the Pinyon-Juniper (PJ) site had the highest overall bias (2.43 °C). In general, biases in the T_{min} model were highest in the winter months, when temperature inversions are most likely to oc-
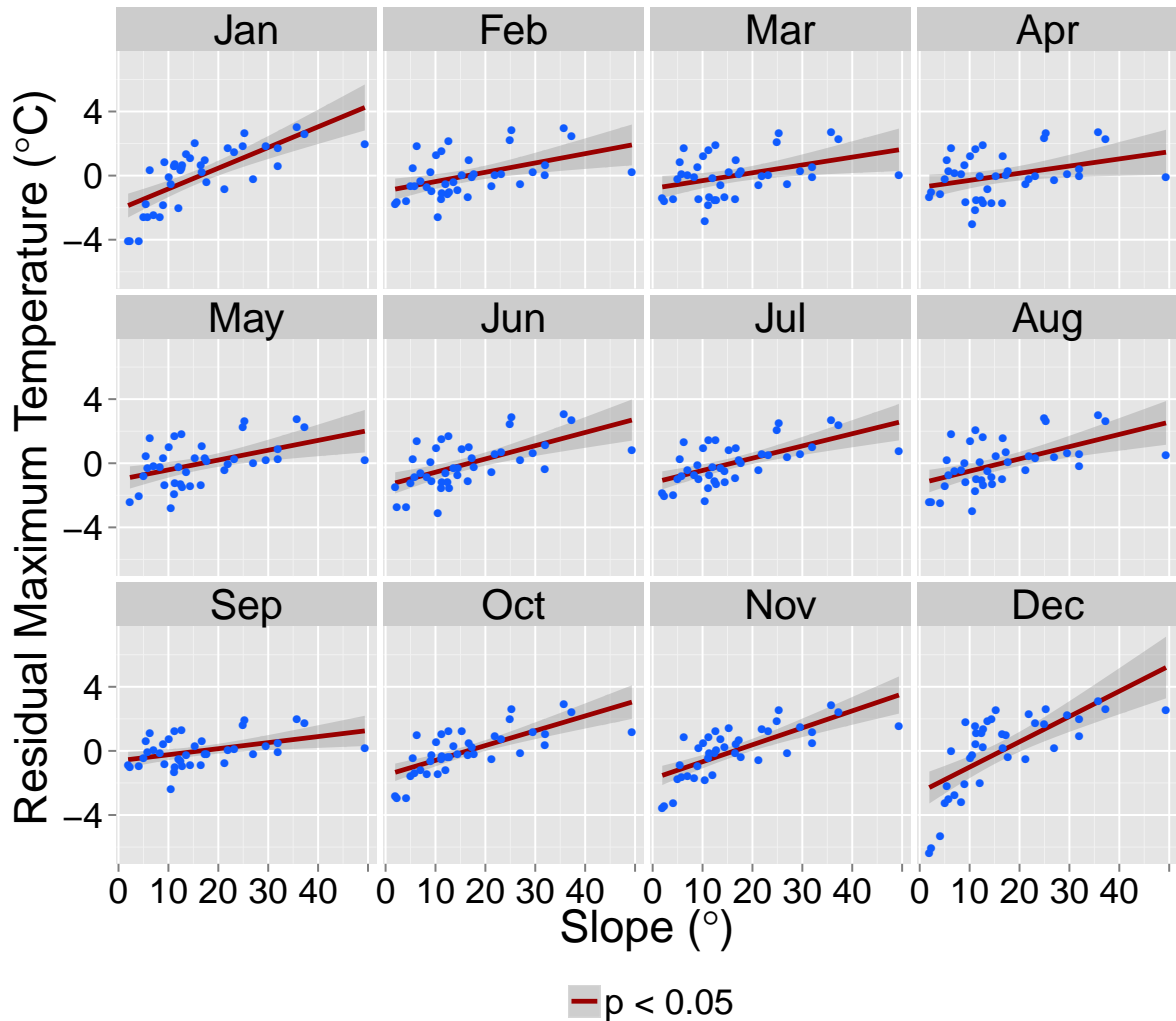
Figure 1.8: Modeled maximum daily temperature averaged over the course of a month between 17 June 2013 and 24 June 2014 expressed as a function of terrain slope (°). Temperature is expressed as the residual of a mixed-effect model fit to the entirety of the SRSN data predicted by elevation with random intercepts by month. Residuals are averaged for each site per month and plotted against the terrain slope at each sensor. The lines are fit by least squares regression. All months were statistically significant at the 0.05 level ($p < 0.05$). The gray shading associated with each regression line indicates the standard error.

cur. The lower elevation minimum temperature predictions show greater variation over time. The higher elevation Montane and Subalpine sites show relatively stable biases throughout the months.

The T_{max} model does not perform as well for the study site as does the T_{min} model (Table 1.3), with an overall bias across sites and times of -1.92 °C. The T_{max} model performs best at the Sage site over the course of the year, with an overall bias of only 0.05 °C. The PJ and Montane sites are both subject to consistently large, negative biases, indicating that the model is under predicting temperature at those sites. The Subalpine site shows the greatest seasonal variation in bias for T_{max} predictions, with more negative biases in the summer months, and biases close to zero in the winter. Overall, the smallest biases for T_{max} are observed at the Sage and Subalpine sites (0.05 and -1.12 °C respectively), while the PJ and Montane sites display higher biases (-3.36 and -3.22 °C respectively).

Mean Absolute Error (MAE) of the T_{min} model was relatively low (1.92 °C, Table 1.4). The site displaying the highest MAE was the Sage site (3.16 °C), while the lowest MAE was observed at the Montane site (1.27 °C). The highest MAE by month at the Sage site is observed during the month of December (6.15 °C), while the lowest MAE is observed at the high elevation Subalpine site in August (0.80 °C). When comparing between sites, the PJ, Montane, and Subalpine sites show relatively stable MAEs throughout time, while the Sage site shows large variations over the course of the year.

MAE of the T_{max} model was higher than the T_{min} model (2.78 °C, Table 1.4), with consistently high MAE values across sites. The site with the lowest T_{max} MAE was the Sage site (2.27 °C). The Spring, and Summer MAE values for the Sage site were relatively consistent across time, while the Fall and Winter MAE values were
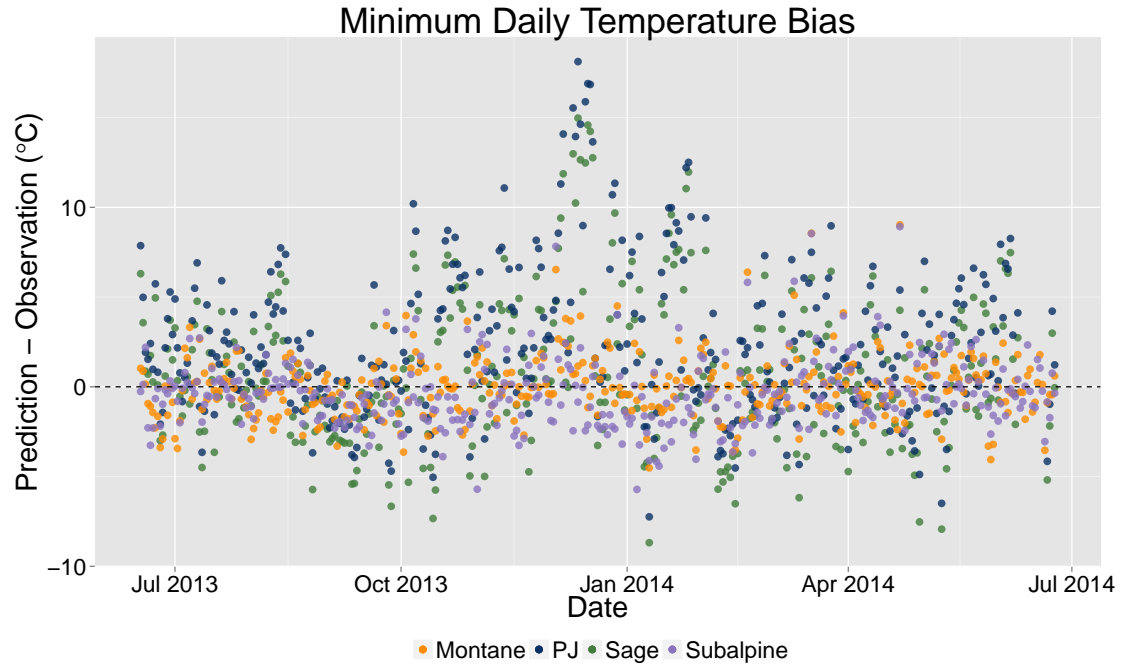
Figure 1.9: Difference between daily minimum temperature (°C) as predicted by the hierarchical mixed-effects model described in text and observed daily minimum temperature at 4 NevCAN stations over time. The Montane site is visualized as orange dots, the Pinyon-Juniper site (PJ) is dark blue, the Sagebrush (Sage) site is dark green, and the Subalpine site is purple. The black horizontal line is placed at the 0 °C mark.

higher and varied more significantly. The Sage site MAE in the month of December was particularly high (4.68 °C), while the MAE for the Sage site in August was much lower (1.33 °C). The month with the highest MAE across sites (Overall in Table 1.4) was December (3.26 °C).

The root mean squared error (RMSE) of the T_{min} model was 2.70 °C (Table 1.5). The site with the highest RMSE was the Sage site (4.18 °C), which was a full 1.9 °C higher than the second highest RMSE at the PJ site (2.28 °C). December at the Sage site stands out with the highest RMSE (8.00 °C), and the sage site again shows lots of variation by month. The PJ, Montane, and Subalpine sites all show relatively stable RMSE values across months compared to the Sage site.
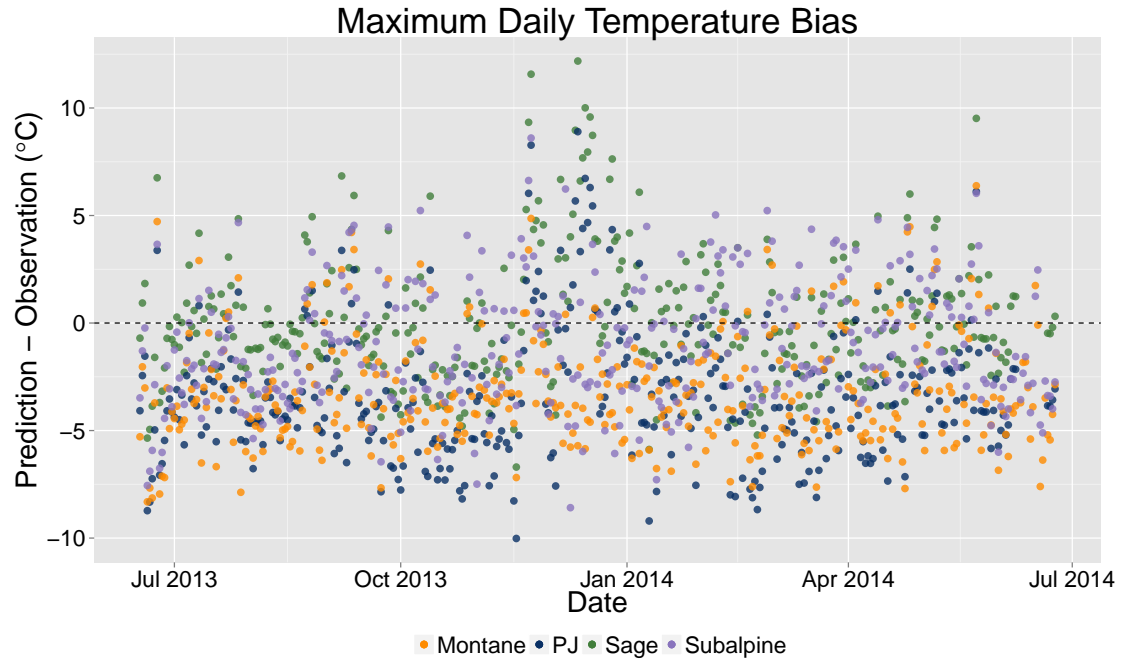
Figure 1.10: Difference between daily maximum temperature (°C) as predicted by the hierarchical mixed-effects model described in text and observed daily maximum temperature at 4 NevCAN stations over time. The Montane site is visualized as orange dots, the Pinyon-Juniper site (PJ) is dark blue, the Sagebrush (Sage) site is dark green, and the Subalpine site is purple. The black horizontal line is placed at the 0 °C mark.

RMSE of the T_{max} model across time and space was slightly higher than the T_{min} model (3.35 °C, Table 1.5). RMSE values are more consistent for the T_{max} model than those of the T_{min} model, with the difference between the highest and lowest RMSE by site equaling 1.09 °C. The Sage site displays higher RMSE values during the winter, and the Montane site displays higher RMSE values in the Spring and Summer. The PJ site is relatively stable across months.

Leave-One-Out Cross Validation

The MSE, RMSE, MAE, and bias of T_{min} and T_{max} (Figure 1.11 and 1.12) were calculated using a leave-one-out cross validation (Table 1.6), and each statistic was

aggregated by Gregorian Calendar month.

The minimum temperature model fits were better during the summer months, as evidenced by lower MSE, RMSE, MAE, and bias values during the summer months relative to the winter. Model bias centers closer to zero during the summer months with less variation (Figure 1.11). The month of greatest variation in minimum temperature bias is December, during which an extreme cold snap was observed. The overall MSE for our T_{min} model was 5.95 °C, the overall RMSE was 2.39 °C, the overall MAE was 1.84 °C, and the overall bias was 0.02 °C (Table 1.6).

The maximum temperature model showed more variation in its performance throughout the year. In general, the summer validation statistics are lower than those values found for Winter (Table 1.6). There is more variation in model bias throughout all months when compared to the T_{min} model (Figure 1.10), with the months of November and December showing the largest amounts of variation. The overall MSE for our T_{max} model was 8.01 °C, the overall RMSE was 2.80 °C, the overall MAE was 2.21 °C, and the overall bias was 0.00 °C.

1.3.4 Temperature Distribution in the SRSN

We have created daily maps of minimum and maximum temperature for the entirety of the SRSN study site during the duration of our 373 day SRSN record. Mean minimum temperature for the month of December 2013 was calculated (Figure 1.13 (a)), as was mean maximum temperature for the month of July 2013 (Figure 1.13 (b)). The pattern of minimum temperature (Figure 1.13 (a)), particularly in the winter months, is highly variable across the landscape. The correlation of the average temperature of each SRSN throughout the time period with elevation
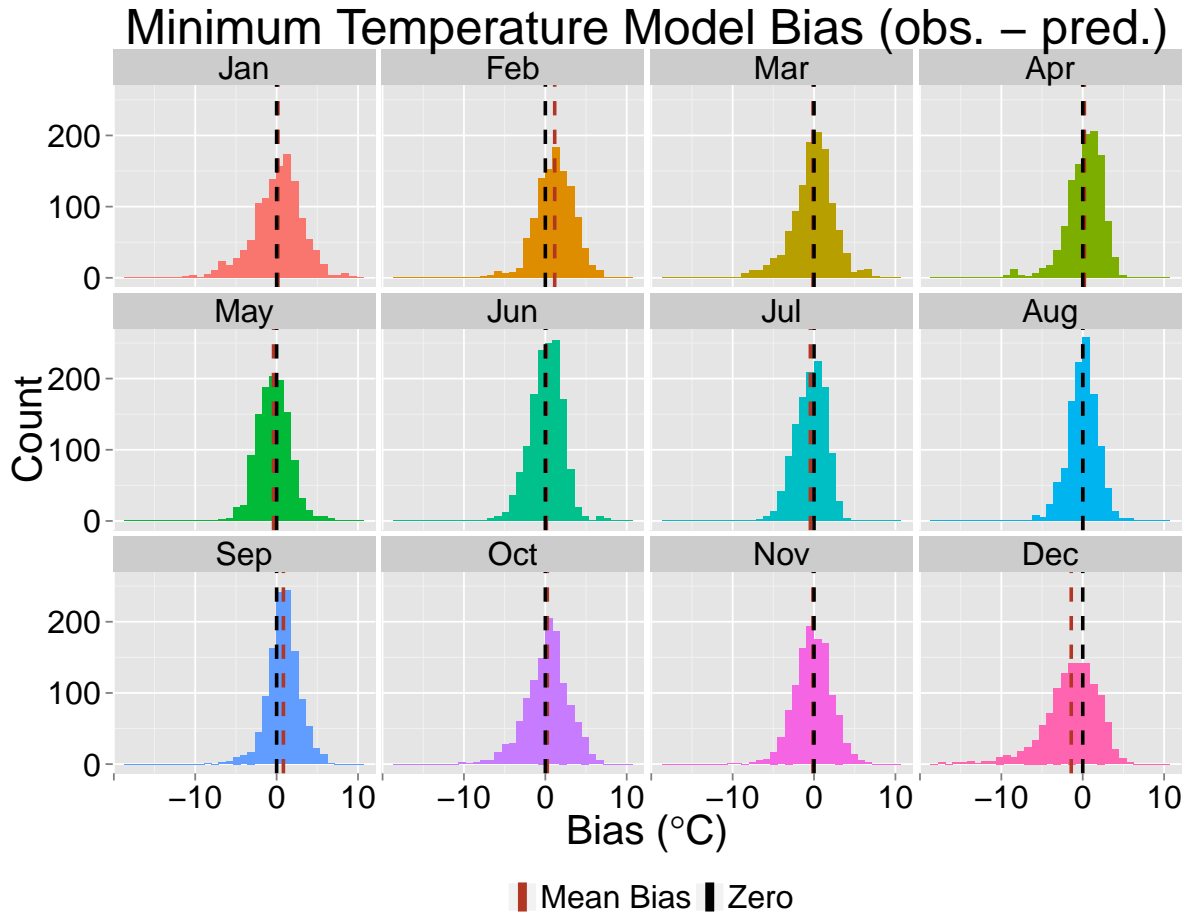
Figure 1.11: Histograms of the minimum temperature model bias for each month of the 373 day SRSN period. Model bias is calculated as the observed temperature minus the predicted temperature. All bias calculations were produced using a leave-one-out cross validation approach, in which the model was fit with all but one sensor, predictions were generated for the location of the sensor, and the observations and predictions for each location were used to calculate bias. These histograms display the bias for all 40 sensor locations and all 373 days of the record, and averages are displayed in Table 1.6. Gray dotted lines are drawn at the 0 °C mark.
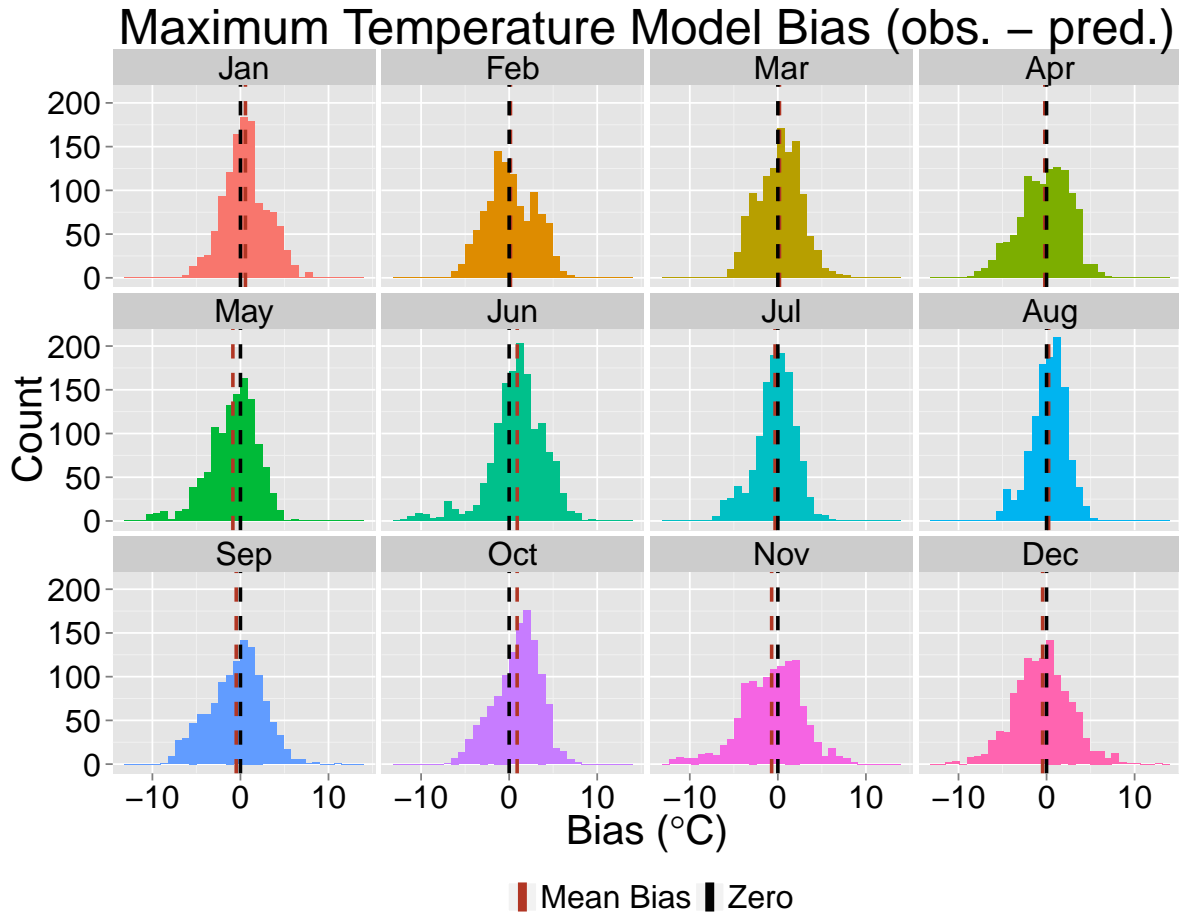
Figure 1.12: Histograms of the maximum temperature model bias for each month of the 373 day SRSN period. Model bias is calculated as the observed temperature minus the predicted temperature. All bias calculations were produced using a leave-one-out cross validation approach, in which the model was fit with all but one sensor, predictions were generated for the location of the sensor, and the observations and predictions for each location were used to calculate bias. These histograms display the bias for all 40 sensor locations and all 373 days of the record, and averages are displayed in Table 1.6. Gray dotted lines are drawn at the 0 °C mark.

is low for T_{min} (r = -0.65), as valley locations are often as cold or colder than the summit of Mount Washington. Maximum temperature averaged across the time series at each sensor location is more strongly correlated with elevation (r = -0.89) (Figure 1.13 (b)).

1.4   Discussion

Our approach to quantify variation in SLP is a novel contribution to the study of topoclimate. We have successfully captured variation in SLP that is relevant to our study site, and inclusion of this information in our study quantified synoptic weather conditions and improved our predictions of T_{max} and T_{min}. Further, we have found that lapse rates are highly variable throughout the seasons. The environmental lapse rate of -6.5 °C km^{-1} is more representative of T_{max} than T_{min}, but an environmental lapse rate is not representative of day-to-day variation in near-surface air temperature.

1.4.1   Variation of Temperature in Complex Topography

This work shows that the environmental lapse rate of -6.5 °C fails to capture daily variation of near-surface air temperature in the Snake Range of Nevada. T_{min} shows substantial variation in values over very short distances (e.g. Figure 1.13 (a)) and within short periods of time (e.g. Figure 1.5). The mosaic of minimum temperatures is very complicated at the landscape scale, and generally does not follow a standard atmospheric lapse rate in our study area. The valley floor is often nearly as cold as the mountain summits, which can have profound implica-
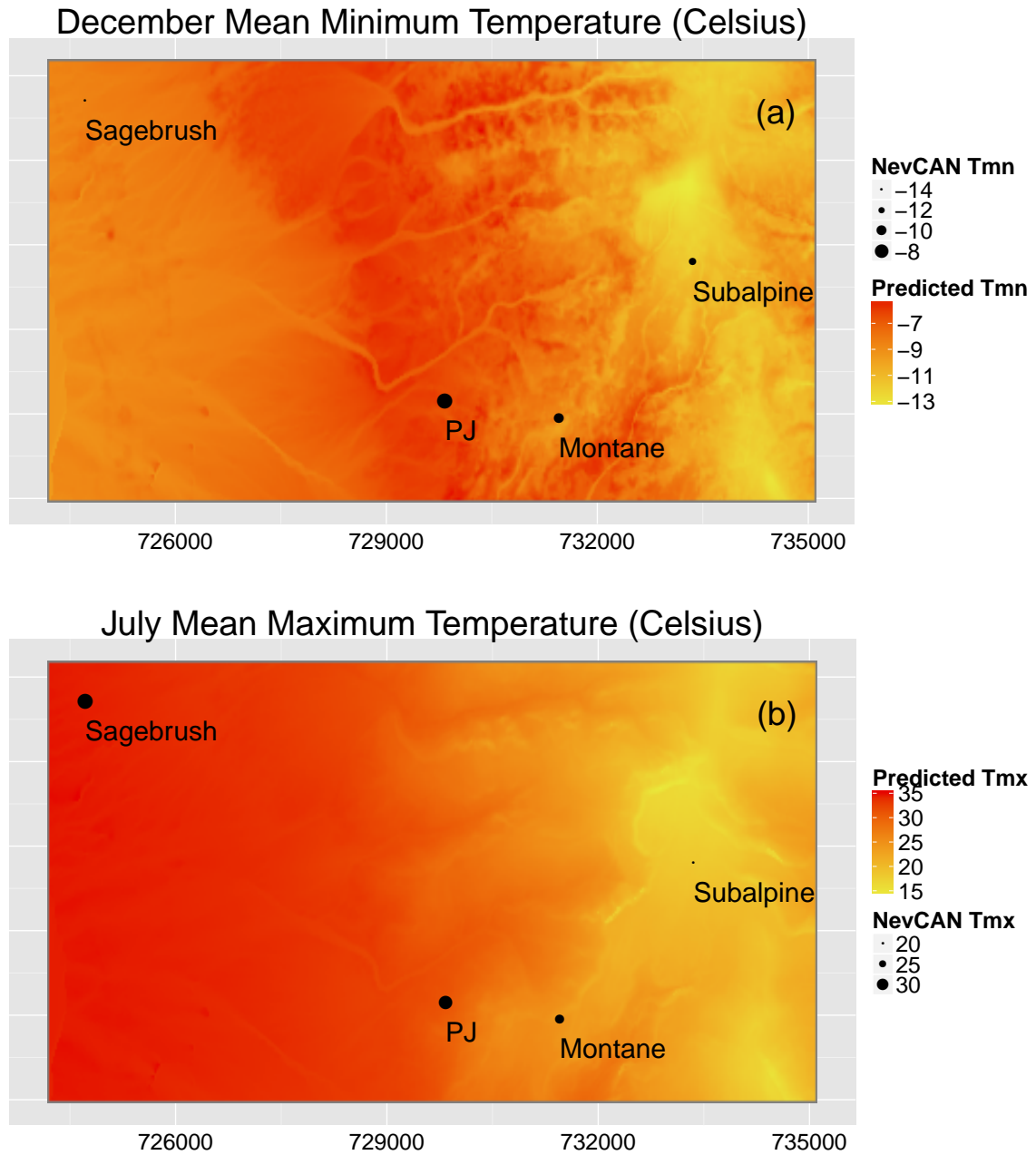
Figure 1.13: Two maps of temperature as predicted by the models described in text. Black dots indicate NevCAN stations and the size of the dot displays mean monthly temperature at that station. These sites are also used as validation sites in this work. Scale and orientation are the same as Figure 1.1. Note that (a) and (b) have different legends and dispaly results from different months. (a) A map of December 2013 average minimum temperature throughout the study site, calculated by taking the mean of daily minimum temperature for the month of December 2013. (b) A map of average maximum temperature for July 2013, calculated by taking the mean of daily maximum temperature predictions for the month of July 2013.

tions for many applications and indicates that environmental lapse rates are not always a satisfactory estimate. This confirms the findings of Blandford et al. (2008) and Pepin et al. (1999). Higher values of percent canopy cover are associated with higher minimum temperatures, indicating that forested areas tend to buffer the region from extreme cold. While this phenomenon has been pointed out repeatedly throughout the literature (e.g. Hough, 1945; Geiger et al., 2009; Barry, 2008), it is often not accounted for in applied research. Moreover, given the arid nature of our study site, vegetation height changes dramatically with elevation, making for an even more complex landscape.

In our study site, T_{max} more frequently displays an environmental lapse rate approaching the standard -6.5 °C km^{-1}. There is generally a consistent decrease in maximum temperature with increasing elevation, and the regional air mass largely dictates what the temperature will be across the landscape. While this is true throughout most of the year, there are still times (particularly in the winter) when T_{max} exhibits inversion conditions. In these cases, even at the hottest point of the day, the valley floor is cooler than higher elevations. Canopy cover also has a moderating effect on maximum temperatures, in that it can often produce cooler temperatures at elevations that would indicate otherwise. The complex spatio-temporal mosaic of both minimum and maximum temperature exhibited here and elsewhere (e.g. Fridley, 2009) is quite difficult to quantify, thus the reliance in the past on simplified methods.

1.4.2 Effects of Synoptic Weather and Seasonality on Near-Surface Temperature

Minimum Temperature

As expected, regional air temperature is the most predictive variable for the daily T_{min} maps in the study area, similar to many works (e.g. Fridley, 2009; Lundquist and Cayan, 2007; Holden et al., 2011a). If the air mass is warm, all sites at the SRSN were slightly warmer than normal. The inverse is also true, where cool regional air masses lead to cooler temperatures across all sites (Figure 1.5).

Minimum temperature exhibited persistent inversions throughout the study period, which is to be expected from other works investigating cold air drainage (e.g. Lundquist et al., 2008). Cold air drainage is a major feature of the minimum temperature climate (Table 1.7). Not only is there a strong effect of elevation in predicting minimum temperature, but there is also quite a large effect of the quadratic of elevation. The quadratic term helps to account for the persistent cold air drainage observed at the study site at some elevations. Minimum temperature tends to display no change in temperature with elevation until approximately 2.3 km, where the decrease in temperature with elevation becomes linear (Figure 1.14 (a)). TCI and slope also help to account for the persistence of cold air drainage at the study site as indicated by their relatively high t values (Table 1.7). These two variables help to identify landscape features that are likely to allow dense, cold air to pool in convex or low slope features (i.e. areas with a high TCI value and/or low slope).

Another interesting feature that is shown here is the mobility of the elevation

Table 1.7: Fixed effect coefficients of hierarchical mixed-effects model of minimum daily temperature for the SRSN.

Coefficient (T_{min})	Estimate	Standard Error	t value
(Intercept)	-36.07	10.27	-3.51
IRRAD	0.002	0.02	0.10
ELEV	32.60	8.46	3.85
ELEV^2	-6.87	1.61	-4.25
PC4	0.13	0.02	5.96
T_{air}	0.88	0.02	55.23
TCI	-0.16	0.07	-2.36
CC	1.05	0.245	4.22
SLOPE	0.04	0.02	2.57
$\cos(2\pi/365 * \text{JDAY})$	-1.78	0.18	-9.69
$\sin(2\pi/365 * \text{JDAY})$	-0.17	0.12	-1.41
ELEV:PC4	-0.09	0.02	-5.24
ELEV^2:PC4	0.01	0.002	4.42
ELEV:CC	-0.80	0.20	-3.96
ELEV^2:CC	0.14	0.04	3.68

where the effect of cold air drainage is observed. The elevation of the cold air drainage layer seems to vary around the 2,000-2,500 m mark (not shown), though the elevation is inconsistent and we did not study its mobility. The PJ NevCAN station is at an elevation of 2,200 m. It is clear that T_{min} model predictions for the PJ station were very inconsistent throughout the year (Figure 1.9). Part of the high bias of the T_{min} model for this particular site is likely due to our inability to estimate how thick the cold air drainage layer is on any given night with the predictor variables presented here. The depth and persistence of these layers at this site calls for more study. The SRSN data are well suited for this, as the inflection point of temperature change with elevation could easily be highlighted with a smoothing average analysis. The variability of the inversion depth would likely be related to the regional weather patterns, time of year, temperature of the air mass, and local winds.
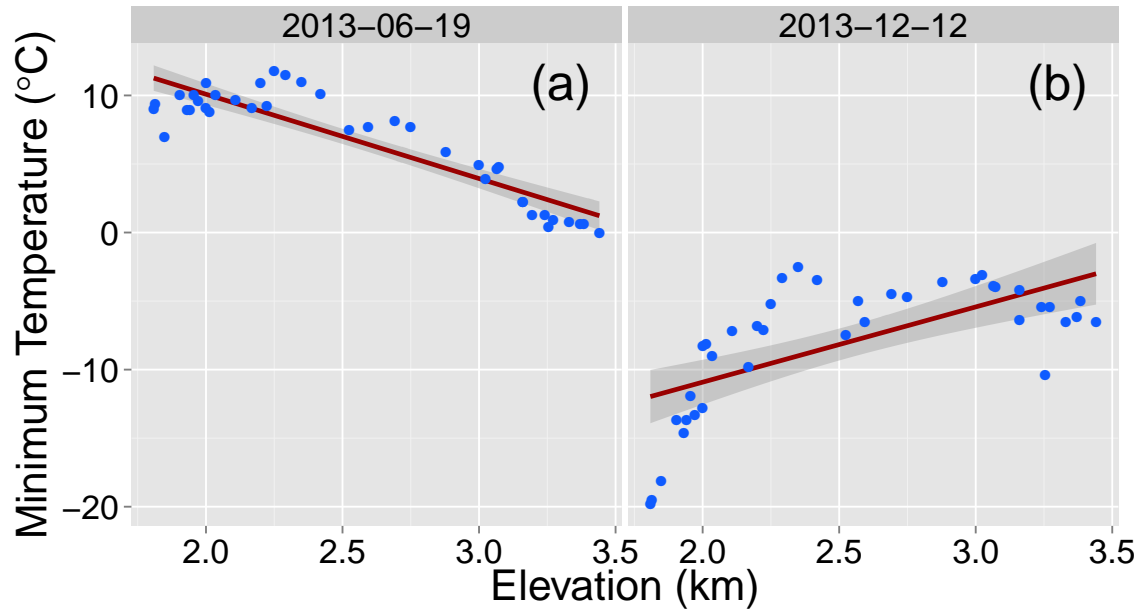
Figure 1.14: Minimum temperature across the 40 sites of the SRSN on two separate days plotted against site elevation. The red lines represent a least squares linear regression model that has been fit to the data, which is often thought of as the lapse rate, and the gray shading associated with the lines indicates standard error from the regression fit. (a) Observations from 19 June 2013, which displays the more typical pattern of T_{min} for the area. Minimum temperature at the lower elevation sites is relatively constant, as cold air drainage occurs on a nearly nightly basis at the site. (b) Minimum temperature recorded by the SRSN plotted against elevation for 12 December 2013. This particular day shows a deep inversion present at the study site, where temperature increases with elevation rather than decreases.

Atmospheric mixing is another important component of the Snake Range climate, particularly in the winter months. Atmospheric mixing refers to the mixing of the near-surface air mass with the greater regional air mass. In the summer months, this can be achieved by convection where the air near the ground surface is warmed and rises (Geiger et al., 2009; Barry, 2008). However, this process is limited in the winter, as the lower sun angles coupled with the complexity of the terrain lead to more of the landscape experiencing "deep shade"; that is to say that these areas receive no direct solar radiation throughout the course of the day. Thus, in the winter, atmospheric mixing is often achieved by the passage of a frontal sys-

tem, which increases winds, instability, and mixing in the regional air mass. As high pressure systems build in the area, cold air drainage persists, limited land surface heating takes place, and thus limited atmospheric mixing occurs. During these high pressure systems, elevation and its quadratic have a complicated relationship with minimum temperature (Figure 1.14 (b)), as the site is under inversions. This phenomenon is pointed out repeatedly in the literature (e.g. Lundquist et al., 2008; Holden et al., 2011b) and well described by our model, and it is quantified by elevation, the quadratic of elevation, and their interaction with PC4. The inclusion of these terms is a first step in attempting to incorporate better information about synoptic weather conditions and their relation to landscape scale temperature mapping, and is one of the most novel contributions of this work.

Maximum Temperature

Regional air temperature is also highly correlated with T_{max} at the study site (Figure 1.5). Maximum temperatures tend to increase and decrease with the regional air mass. However, the range of maximum temperature values observed on a given day varies by season and synoptic weather conditions. This result appears to be consistent with Fridley (2009).

The lapse rate of maximum temperatures is much more consistent than that of minimum temperature (Figure 1.15 (a)), as cold air drainage is not a major component of the daytime climate at our study site, again confirming the results of Blandford et al. (2008). There is a strong effect of elevation and its quadratic interacting with the sine and cosine waves that were fit to the model, which indicates that the effects of elevation and its quadratic change with the seasons (Table 1.8). This is easy to reconcile, as changes in the season also bring about changes in the

sun angle. Much like in minimum temperature, high pressure coupled with low sun angles (hence low atmospheric mixing) during the winter months can lead to inversions in maximum daily temperature (Figure 1.15 (b)). The cosine curve better explains the seasonality of our study site. It has a maximum value in the winter and a minimum value in the summer, indicating that the hydro-climatic regime of the region is centered on winter and summer. To further explain the seasonality of inversions, the maximum temperature model includes an interaction term of the cosine wave with TCI at the study site. This accounts for the fact that TCI is more predictive of T_{max} in our study site during the winter months, as this is when inversions are most likely to occur.

Table 1.8: Fixed effect coefficients of hierarchical mixed-effects model of maximum daily temperature for the SRSN.

Coefficient (T_{max})	Estimate	Standard Error	t value
(Intercept)	31.98	6.66	4.80
T_{air}	0.87	0.02	35.68
IRRAD	0.58	0.03	21.96
PC4	-0.01	0.00	-5.62
ELEV	-10.91	5.49	-1.99
ELEV^2	0.37	1.03	0.36
TCI	-0.07	0.07	-1.00
$\cos(2\pi/365 * \text{JDAY})$	-0.70	0.96	-0.73
$\sin(2\pi/365 * \text{JDAY})$	-0.43	0.96	-0.45
SLOPE	0.03	0.02	1.95
CC	0.01	0.01	1.13
TCI:$\cos(2\pi/365 * \text{JDAY})$	0.02	0.01	3.34
TCI:$\sin(2\pi/365 * \text{JDAY})$	0.00	0.01	0.21
ELEV:$\cos(2\pi/365 * \text{JDAY})$	-3.61	0.71	-5.06
ELEV^2:$\cos(2\pi/365 * \text{JDAY})$	1.08	0.14	7.75
ELEV:$\sin(2\pi/365 * \text{JDAY})$	1.13	0.72	1.57
ELEV^2 :$\sin(2\pi/365 * \text{JDAY})$	-0.32	0.14	-2.26

Aside from some extreme winter values (Figure 1.10, December 2013), the bias in the T_{max} model is relatively consistent. This is likely due to the stability and pre-

dictability of maximum temperatures throughout most of the year. Atmospheric lapse rates are reasonable estimates of the distribution of maximum temperature throughout a landscape due to the stability of T_{max}. However, this overly simple approach still does not account for site specific differences in solar irradiance, canopy cover, and other important variables, thus trade-offs between highly detailed temperature maps and ease of construction should be considered on a project by project basis.

1.4.3   Effects of Landscape Features on Near-Surface Temperature

Minimum Temperature

Elevation is certainly one of the most important components of T_{min} distribution in the area, but the relationship is not a simple linear one. Our model accounts for numerous ways in which relationships between elevation and T_{min} vary throughout the landscape (Table 1.7), and we are likely still missing part of the picture. Allowing a quadratic term of elevation helps to account for the persistent cold air drainage encountered at our site, and will likely apply to other sites in the western United States or any arid, mid-latitude site. Elevation and its quadratic also exhibit a strong interaction with canopy cover at the study site. We speculate that this interaction term helps to account for the varying structure of the canopy, as it changes dramatically at our study site with elevation.

There is a very weak effect of IRRAD on T_{min} at our study site. By the time daily minimum temperature occurs at our site, the effects of daily insolation have diminished. Canopy cover has a strong effect on minimum temperature at our

study site, as thicker canopies tend to insulate the near-surface climate from extreme temperature swings, which is a well studied process (e.g. Hough, 1945). Our study confirms that this process is taking place at the Snake Range. One of the strongest landscape effects is the shape of the terrain and its effect on cold air drainage. Our model accounts for this effect by including TCI and terrain slope as model terms. These two variables have relatively strong effects. The effect of TCI is negative, as areas with high TCI values are typically concavities in the landscape. These concavities are areas that are likely to allow more dense cold air to accumulate, thus will generally display a colder climate than would areas with a more convex landscape. Slope has a positive effect on T_{min}, as areas with higher slope values will "clear" the more dense cold air rapidly as it cools, helping to keep these areas near the same temperature as the regional air mass. This result is consistent with Lundquist et al. (2008), as they found terrain slope to be an important factor in identifying areas likely to accumulate cold air.

Maximum temperature

Elevation has a strong effect on T_{max} in the Snake Range, with a relatively small effect displayed by the quadratic of elevation (e.g. Figure 1.15 (a)). As elevation data are readily available and highly predictive of temperature, predicting T_{max} is relatively simple. However, this relationship is not stationary with time, as in the winter months, temperature inversions from the valley floor all the way to the mountain summit are not uncommon (e.g. Figure 1.15 (b)). Thus, if the application requires detailed information about temperature or requires the ability to describe when and how deep inversions are in the study site, a method similar to what was employed in this study is suggested.
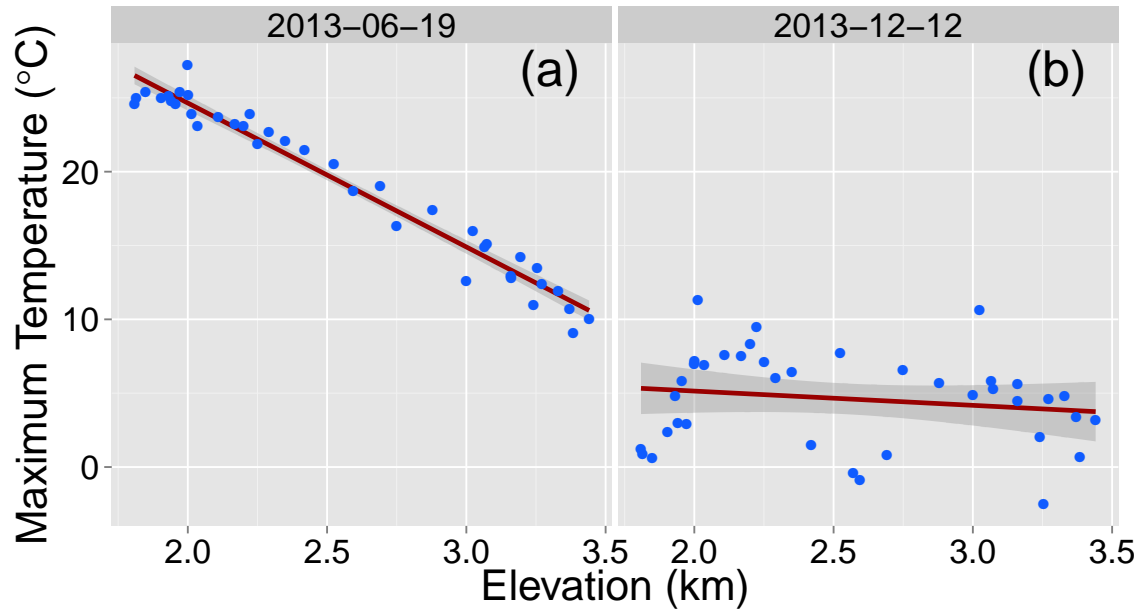
Figure 1.15: Maximum temperature across the 40 sites of the SRSN on two separate days plotted against site elevation. The red lines represent a least squares linear regression model that has been fit to the data, which is often thought of as the lapse rate, and the gray shading associated with the lines indicates standard error from the regression fit. (a) Maximum daily temperature from 2013 June 19. This displays a typical maximum temperature observation at the site, where maximum temperature decreases linearly with decreasing elevation. Note the relatively small standard error, as elevation is largely representative of maximum temperature on this date. (b) Maximum daily temperature from 2013 December 12, which shows a persistent inversion occurring at the site. As you increase elevation, there is a very slight decrease in maximum temperature for that day.

Incoming solar radiation has a very large effect on maximum temperature at the sites in the SRSN (Table 1.8). The effects are comparable to those found by Fridley (2009), but a direct comparison between the two studies is tenuous. Fridley (2009) allowed IRRAD to interact with other variables, while this study did not. The relationship between T_{max} and IRRAD is intuitive, with high solar radiation equating to high maximum temperature and vice versa. Theoretical incoming solar radiation can be easily modeled within a GIS framework, making this important variable available to all applications. However, to better understand the

dynamics of how irradiance effects maximum temperature, it would be ideal to include information on cloud cover. On cloudy days or during the formation of summer thunderstorms, the actual incoming solar radiation could greatly diverge from the theoretical value calculated with GIS despite our study site having a large proportion of sunny days. Some scientists have gone as far as to exclude irradiance in their studies for this reason (e.g. Ashcroft and Gollan, 2011), but given our results, it is certainly worth inclusion in arid regions.

As temperature inversions of T_{max} occur at our study site, particularly in the winter (not shown), we have included an interaction term of TCI, elevation, and the quadratic of elevation with the sine and cosine waves that describe seasonal variation at our study site. Again, the cosine wave seems to better fit the timing of seasonality at our site. Allowing our landscape variables to interact with the day of year helps to account for the differing effect of these landscape variables through time. While TCI and ELEV^2 are both important variables to help describe inversion conditions, they do not contribute much information to the distribution of maximum temperature over the landscape during normal conditions. Ideally a better description of the seasonality at our site can be achieved, which will allow for more accurate mapping of the timing and distribution of inversions in T_{max} in the Snake Range.

1.4.4   Refinements and future work

The availability and low cost of modern microsensors such as the LogTag Trix 16 units used in this study have led to a proliferation of landscape-scale temperature studies. These studies will benefit from some form of standardization, as it is cur-

rently quite difficult to compare results. Some researchers place their sensors in trees as we have (Lundquist and Cayan, 2007; Lookingbill and Urban, 2003), some place their sensors under the soil surface (Ford et al., 2013), some use PVC housings for radiation shields (Fridley, 2009; Ashcroft and Gollan, 2011), and others make their own in house radiation shields (Holden et al., 2013, 2011a; Hubbart, 2005). The amount of measurement error and bias that is contributed by these different methods needs to be accounted for when quantitatively comparing results, but the general drivers of near-surface air temperature in different geographic regions likely hold true.

It is important to note that while this model effectively describes near-surface temperature in the Snake Range throughout the period of record, researchers must be cautious if they are to extrapolate such models to larger landscapes or different time periods. While the use of the NCEP Reanalysis 1 data to describe synoptic conditions at our study site makes the model well suited for calculating temperature maps of past conditions, it is worth noting that the near-ground climate of the past may be very different than the near-ground climate of the present. This exercise would certainly hold some merit in a first glimpse of a detailed climate history for the area, but many of the assumptions made by this work will likely break in different points in space or time.

APPENDIX A

HIERARCHICAL MIXED-EFFECTS MODEL FITTING

A.1   General Fitting Procedure

Construction of multilevel models such as those employed here requires assessing the variance at each level of the model. This is because more complex model structures are only supported within this framework if they have relatively high variance and degrees of freedom on a particular level.

Level One of our models includes daily fluctuations of the regional air mass temperature (T_{air}), SLP patterns in the study region (PC4), clear sky irradiance (IRRAD), other seasonal variation (sine and cosine periodic functions), and any interactions between these variables. The model includes 373 days of values at level one, thus most of the variance and most of the degrees of freedom come from this level. Level One includes factors that influence site specific temperature during time t at location i. A forward fitting procedure was used, in which only the variables thought to be most physically relevant are included in the first model. This model was tested with log likeliehood via AIC against alternative models which included varying forms of random effects and additional predictor variables for date until a "best" model (as determined by AIC) that is physically relevant is achieved. Each model on Level 1 can include a random effect that varies over the course of the 373 days, helping to account for noise and serial autocorrelation in the time series. In our final models, we employed a random intercept by date.

Next, we address the level 2 variables in a similar manner. Level two variables describe spatial variation of maximum and minimum temperature throughout the study site, such that the predictor varies at each location i. Forward model fitting procedures were employed to determine the most suitable Level Two of the model.

Next, Level One coefficients can be modeled at Level Two, such that interactions between temporal and spatial predictors can occur (e.g. the effect of elevation can vary with differing levels of PC4). Each component of Level 2 can also include random effects of the slope and/or intercept to account for errors between sites. In our final model, we included a random intercept by sensor location and a random slope by elevation for each day to account for the variability of lapse rates at the site. Once a full model was determined by comparing competing models with log-likelihood tests, we removed random effects terms to determine their significance. After demonstrating the statistical significance of these terms, we tested for temporal autocorrelation in the residuals of the models by comparing the full model to the same model including an exponential decay autocorrelation term (Pinheiro et al., 2014), and found that the random terms accounted for enough of the temporal autocorrelation that the more complicated covariance structure was not justified by log-likelihood testing and AIC values.

A.2 Minimum Temperature Model

Our final hierarchical mixed-effects linear regression model for T_{min} where i indicates some location, t indicates some day, and $minT_{it}$ indicates the minimum daily

temperature from that day and that location was as follows:

$$
\begin{aligned}
minT_{it} =& \beta_{0it} + \beta_{1it}TAIR + \beta_{2it}IRRAD + \beta_{3t}PC4+ \\
& \beta_{4t}cos(2\pi/365 * JDAY) + \beta_{5t}sin(2\pi/365 * JDAY)+ \\
& \beta_{6it}ELEV + \beta_{7it}ELEV^2 + \beta_{8it}TCI+ \\
& \beta_{9it}CC + \beta_{10it}SLOPE + \beta_{11it}PC4 \times ELEV+ \\
& \beta_{12it}PC4 \times ELEV^2 + \beta_{13it}ELEV \times CC+ \\
& \beta_{14it}ELEV^2 \times CC + u_{00i} + u_{00t} + w_{00it}ELEV+ \\
& w_{01it}ELEV^2 + \epsilon_{it}
\end{aligned}
\tag{A.1}
$$

which includes random intercepts for site and date, and random slopes for elevation and its quadratic each day of the record. Fixed effects terms include regional air mass (TAIR or T_{air} in text), irradiance, PC4, periodic sine and cosine functions, elevation, the quadratic of elevation, TCI, canopy cover, slope, the interaction of PC4, elevation, and the quadratic of elevation, and finally the interaction of CC, elevation, and the quadratic of elevation. The final term of the model is normally distributed error.

A.3 Maximum Temperature Model

The final hierarchical mixed-effects linear regression model for T_{max} at some location i and some time t to predict the maximum temperautre, $maxT_{it}$, at that

location during that time is:

$$
\begin{aligned}
maxT_{it} =& \beta_{0it} + \beta_{1it}TAIR + \beta_{2it}IRRAD + \beta_{3t}PC4+ \\
& \beta_{4t}cos(2\pi/365*JDAY) + \beta_{5t}sin(2\pi/365*JDAY)+ \\
& \beta_{6it}ELEV + \beta_{7it}ELEV^2 + \beta_{8it}TCI+ \\
& \beta_{9it}CC + \beta_{10it}SLOPE + \beta_{11it}TCI \times sin(2\pi/365*JDAY)+ \\
& \beta_{12it}TCI \times cos(2\pi/365*JDAY) + \beta_{13it}ELEV \times sin(2\pi/365*JDAY)+ \\
& \beta_{14it}ELEV \times cos(2\pi/365*JDAY) + \beta_{15it}ELEV^2 \times sin(2\pi/365*JDAY)+ \\
& \beta_{16it}ELEV^2 \times cos(2\pi/365*JDAY) + u_{00i} + u_{00t} + w_{00it}ELEV+ \\
& w_{01it}ELEV^2 + \epsilon_{it}
\end{aligned}
$$

$$(A.2)$$

This model includes random intercepts for site and date, as well as random slopes for elevation and its quadratic for each day. Fixed effects include regional air temperature, irradiance, PC4, elevation, the quadratic of elevation, TCI, periodic sine and cosine functions (seasonality), slope, canopy cover, the interaction of TCI with seasonality, the interaction of elevation and seasonality, and the interaction of the quadratic of elevation and seasonality. The final term of the model is normally distributed error.

BIBLIOGRAPHY

Adams, H. D., M. Guardiola-Claramonte, G. A. Barron-Gafford, J. C. Villegas, D. D. Breshears, C. B. Zou, P. A. Troch, and T. E. Huxman, 2009: Temperature sensitivity of drought-induced tree mortality portends increased regional die-off under global-change-type drought. *Proceedings of the National Academy of Sciences of the United States of America*, **106 (17)**, 7063–6, doi:10.1073/pnas.0901438106, URL http://www.pubmedcentral.nih.gov/articlerender.fcgi?artid=2678423&tool=pmcentrez&rendertype=abstract.

Ashcroft, M. B., and J. R. Gollan, 2011: Fine-resolution (25 m) topoclimatic grids of near-surface (5 cm) extreme temperatures and humidities across various habitats in a large (200 x 300 km) and diverse region. *International Journal of Climatology*, n/a–n/a, doi:10.1002/joc.2428, URL http://doi.wiley.com/10.1002/joc.2428.

Ashcroft, M. B., J. R. Gollan, D. I. Warton, and D. Ramp, 2012: A novel approach to quantify and locate potential microrefugia using topoclimate, climate stability, and isolation from the matrix. *Global Change Biology*, **18 (6)**, 1866–1879, doi:10.1111/j.1365-2486.2012.02661.x, URL http://doi.wiley.com/10.1111/j.1365-2486.2012.02661.x.

Barry, R. G., 2008: *Mountain Weather and Climate*. 3rd ed., Cambridge University Press, New York.

Bates, D., M. Machler, B. M. Bolker, and S. C. Walker, 2014: Fitting linear mixed-effects models using lme4. *Journal of Statistical Software*, URL http://CRAN.R-project.org/package=lme4.

Bivand, R., T. Keitt, and B. Rowlingson, 2014: *rgdal: Bindings for the Geospatial Data*

Abstraction Library. URL http://CRAN.R-project.org/package=rgdal, r package version 0.9-1.

Bivand, R. S., E. Pebesma, and V. Gomez-Rubio, 2013: *Applied Spatial Data Analysis with R*. 2nd ed., Springer, New York.

Blandford, T. R., K. S. Humes, B. J. Harshburger, B. C. Moore, V. P. Walden, and H. Ye, 2008: Seasonal and Synoptic Variations in Near-Surface Air Temperature Lapse Rates in a Mountainous Basin. *Journal of Applied Meteorology and Climatology*, **47 (1)**, 249–261, doi:10.1175/2007JAMC1565.1, URL http://journals. ametsoc.org/doi/abs/10.1175/2007JAMC1565.1.

Cabrera, H. M., F. Rada, and L. Cavieres, 1998: Effects of temperature on photosynthesis of two morphologically contrasting plant species along an altitudinal gradient in the tropical high Andes. *Oecologia*, **114 (2)**, 145–152, doi: 10.1007/s004420050430, URL http://link.springer.com/10.1007/s004420050430.

Crimmins, S. M., S. Z. Dobrowski, J. a. Greenberg, J. T. Abatzoglou, and A. R. Mynsberge, 2011: Changes in climatic water balance drive downhill shifts in plant species' optimum elevations. *Science (New York, N.Y.)*, **331 (6015)**, 324–7, doi:10.1126/science.1199040, URL http://www.ncbi.nlm.nih.gov/pubmed/21252344.

Daly, C., M. Halbleib, and J. Smith, 2008: Physiographically sensitive mapping of climatological temperature and precipitation across the conterminous United States. *International Journal of Climatology of Climatology*, doi:10.1002/joc, URL http://onlinelibrary.wiley.com/doi/10.1002/joc.1688/full.

Diaz, H., M. Grosjean, and L. Graumlich, 2003: *Climate variability and change in*

high elevation regions: past, present and future, Vol. 2001. 1–4 pp., URL http://link.springer.com/chapter/10.1007/978-94-015-1252-7_1.

Dobrowski, S. Z., 2011: A climatic basis for microrefugia: the influence of terrain on climate. *Global Change Biology*, **17 (2)**, 1022–1035, doi:10.1111/j.1365-2486.2010.02263.x, URL http://doi.wiley.com/10.1111/j.1365-2486.2010.02263.x.

Dobrowski, S. Z., J. T. Abatzoglou, J. a. Greenberg, and S. Schladow, 2009: How much influence does landscape-scale physiography have on air temperature in a mountain environment? *Agricultural and Forest Meteorology*, **149 (10)**, 1751–1758, doi:10.1016/j.agrformet.2009.06.006, URL http://linkinghub.elsevier.com/retrieve/pii/S0168192309001488.

ESRI, 2014: *ArcGIS 10.1*. URL http://resources.arcgis.com/en/help/main/10.1/index.html#//00nv0000000v000000.

Ford, K. R., A. K. Ettinger, J. D. Lundquist, M. S. Raleigh, and J. Hille Ris Lambers, 2013: Spatial heterogeneity in ecologically important climate variables at coarse and fine scales in a high-snow mountain landscape. *PloS one*, **8 (6)**, e65 008, doi:10.1371/journal.pone.0065008, URL http://www.pubmedcentral.nih.gov/articlerender.fcgi?artid=3676384&tool=pmcentrez&rendertype=abstract.

Fridley, J. D., 2009: Downscaling climate over complex terrain: High finescale (<1000 m) spatial variation of near-ground temperatures in a montane forested landscape (Great Smoky Mountains). *Journal of Applied Meteorology and Climatology*, **48**, 1033–1049, doi:10.1175/2008JAMC2084.1.

Fry, J., G. Xian, J. Dewitz, C. Homer, L. Yang, C. Barnes, N. Herold, and J. Wickham, 2011: Completion of the 2006 national land cover database for the con-

terminous united states. *PE&RS*, **77 (9)**, 858–864, URL http://www.mrlc.gov/downloadfile2.php?file=September2011PERS.pdf.

Geiger, R., R. H. Aron, and P. Todhunter, 2009: *The Climate Near the Ground*. 7th ed., Rowman & Littlefield Publishers.

GRASS Development Team, 2012: *Geographic Resources Analysis Support System (GRASS GIS) Software*. USA, Open Source Geospatial Foundation, URL http://grass.osgeo.org.

Hannachi, A., I. T. Jolliffe, and D. B. Stephenson, 2007: Empirical orthogonal functions and related techniques in atmospheric science: A review. *International Journal of Climatology*, **27**, 1119–1152, doi:10.1002/joc, URL http://onlinelibrary.wiley.com/doi/10.1002/joc.1499/full.

Hijmans, R. J., 2014: *raster: raster: Geographic data analysis and modeling*. URL http://CRAN.R-project.org/package=raster, r package version 2.3-12.

Hijmans, R. J., S. E. Cameron, J. L. Parra, P. G. Jones, and A. Jarvis, 2005: Very high resolution interpolated climate surfaces for global land areas. *International Journal of Climatology*, **25 (15)**, 1965–1978, doi:10.1002/joc.1276, URL http://doi.wiley.com/10.1002/joc.1276.

Holden, Z. A., J. T. Abatzoglou, C. H. Luce, and L. S. Baggett, 2011a: Empirical downscaling of daily minimum air temperature at very fine resolutions in complex terrain. *Agricultural and Forest Meteorology*, **151 (8)**, 1066–1073, doi:10.1016/j.agrformet.2011.03.011, URL http://linkinghub.elsevier.com/retrieve/pii/S0168192311001080.

Holden, Z. A., M. A. Crimmins, S. A. Cushman, and J. S. Littell, 2011b: Empirical modeling of spatial and temporal variation in warm season nocturnal

air temperatures in two North Idaho mountain ranges, USA. *Agricultural and Forest Meteorology*, **151 (3)**, 261–269, doi:10.1016/j.agrformet.2010.10.006, URL http://linkinghub.elsevier.com/retrieve/pii/S0168192310002819.

Holden, Z. A., A. E. Klene, R. F. Keefe, and G. G. Moisen, 2013: Design and evaluation of an inexpensive radiation shield for monitoring surface air temperatures. *Agricultural and Forest Meteorology*, **180**, 281–286, doi:10.1016/j.agrformet.2013. 06.011, URL http://linkinghub.elsevier.com/retrieve/pii/S016819231300169X.

Horel, J. D., and X. Dong, 2010: An Evaluation of the Distribution of Remote Automated Weather Stations (RAWS). *Journal of Applied Meteorology and Climatology*, **49 (7)**, 1563–1578, doi:10.1175/2010JAMC2397.1, URL http://journals.ametsoc. org/doi/abs/10.1175/2010JAMC2397.1.

Hough, A. F., 1945: Frost Pocket and Other Microclimates in Forests of the Northern Allegheny Plateau. *Ecology*, **26 (3)**, 235–250.

Hubbart, K. K. P. R. L. T. S. A., J.A., 2005: Cold air drainage and modeled nocturnal leaf water potential in complex forested terrain. *Tree Physiology*, **27**, 631–639.

Jin, S., L. Yang, P. Danielson, C. Homer, J. Fry, and G. Xian, 2013: A comprehensive change detection method for updating the national land cover database to circa 2011. *Remote Sensing of Environment*, **132**, 159–175, URL http://www. sciencedirect.com/science/article/pii/S0034425713000242.

Kalnay, E., and Coauthors, 1996: The NCEP/NCAR 40-Year Reanalysis Project. *Bulletin of the American Meteorological Society*, **77 (3)**, 437–471.

Lookingbill, T., and D. Urban, 2003: Spatial estimation of air temperature differences for landscape-scale studies in montane environments. *Agricultural and*

Forest Meteorology, **114**, 141–151, URL http://www.sciencedirect.com/science/article/pii/S016819230200196X.

Lundquist, J. D., and D. R. Cayan, 2007: Surface temperature patterns in complex terrain: Daily variations and long-term change in the central Sierra Nevada, California. *Journal of Geophysical Research*, **112 (D11)**, 1–15, doi:10.1029/2006JD007561, URL http://www.agu.org/pubs/crossref/2007/2006JD007561.shtml.

Lundquist, J. D., and B. Huggett, 2008: Evergreen trees as inexpensive radiation shields for temperature sensors. *Water Resources Research*, **44 (October)**, 1–5, doi:10.1029/2008WR006979, URL http://www.agu.org/pubs/crossref/2008/2008WR006979.shtml.

Lundquist, J. D., N. Pepin, and C. Rochford, 2008: Automated algorithm for mapping regions of cold-air pooling in complex terrain. *Journal of Geophysical Research*, **113 (D22)**, D22 107, doi:10.1029/2008JD009879, URL http://doi.wiley.com/10.1029/2008JD009879.

Martinec, J., and a. Rango, 1986: Parameter values for snowmelt runoff modelling. *Journal of Hydrology*, **84 (3-4)**, 197–219, doi:10.1016/0022-1694(86)90123-X, URL http://linkinghub.elsevier.com/retrieve/pii/002216948690123X.

McCune, B., and D. Keon, 2002: Equations for potential annual direct incident radiation and heat load. *Journal of vegetation science*, **(1966)**, 603–606, URL http://onlinelibrary.wiley.com/doi/10.1111/j.1654-1103.2002.tb02087.x/abstract.

Mensing, S., and Coauthors, 2013: A Network for Observing Great Basin Climate Change. *Eos, Transactions American Geophysical Union*, **94 (11)**, 105–106, doi:10.1002/2013EO110001, URL http://doi.wiley.com/10.1002/2013EO110001.

Millar, C. I., N. L. Stephenson, and S. L. Stephens, 2007: Climate change and forests of the future: Managing in the face of uncertainty. **17 (8)**, 2145–2151.

Myrick, D. T., and J. D. Horel, 2008: Sensitivity of Surface Analyses over the Western United States to RAWS Observations. *Weather and Forecasting*, **23 (1)**, 145–158, doi:10.1175/2007WAF2006074.1, URL http://journals.ametsoc.org/doi/abs/10.1175/2007WAF2006074.1.

Pebesma, E., 2012: spacetime: Spatio-Temporal Data in R. *Journal of Statistical Software*, **51 (7)**, 1–30, URL http://www.jstatsoft.org/v51/i07/.

Pepin, N., D. Benham, and K. Taylor, 1999: Modeling lapse rates in the maritime uplands of northern england: Implications for climate change. *Arctic, Antarctic, and Alpine Research*, **31 (2)**, 151–164.

Pepin, N. C., C. Daly, and J. Lundquist, 2011: The influence of surface versus free-air decoupling on temperature trend patterns in the western United States. *Journal of Geophysical Research*, **116 (D10)**, D10 109, doi:10.1029/2010JD014769, URL http://doi.wiley.com/10.1029/2010JD014769.

Pinheiro, J., and D. Bates, 2000: *Mixed-Effects Models in S and S-PLUS*. 1st ed., Springer, New York.

Pinheiro, J., D. Bates, S. DebRoy, D. Sarkar, and R Core Team, 2014: *nlme: Linear and Nonlinear Mixed Effects Models*. URL http://CRAN.R-project.org/package=nlme, r package version 3.1-118.

R Core Team, 2014: *R: A Language and Environment for Statistical Computing*. Vienna, Austria, R Foundation for Statistical Computing, URL http://www.R-project.org/.

Rolland, C., 2003: Spatial and seasonal variations of air temperature lapse rates in Alpine regions. *Journal of Climate*, **16**, 1032–1046, URL http://journals.ametsoc.org/doi/abs/10.1175/1520-0442(2003)016⟨1032:SASVOA⟩2.0.CO;2.

Steinhauser, F. W., 1967: Methods of Evaluation and Drawing of Climate Maps in Mountainous Countries. *Archiv fur Meteorologie, Geophysik und Bioklimatologie*, **15 (4)**, 329–358.

Thornton, P. E., S. W. Running, and M. A. White, 1997: Generating surfaces of daily meteorological variables over large regions of complex terrain. *Journal of Hydrology*, **190 (3-4)**, 214–251, doi:10.1016/S0022-1694(96)03128-9, URL http://linkinghub.elsevier.com/retrieve/pii/S0022169496031289.